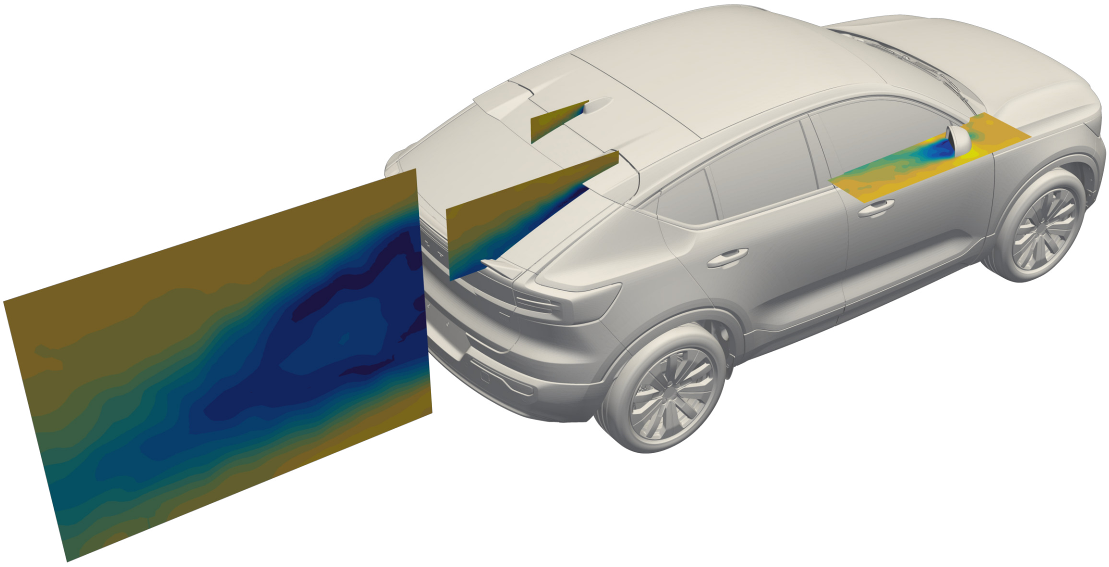

Flow visualization techniques for full-scale test objects in a wind tunnel

Evaluation of a novel flow visualization technique

Master's thesis in Mobility Engineering

CLEMENS STEINKE

DEPARTMENT OF MECHANICS AND MARITIME SCIENCES
CHALMERS UNIVERSITY OF TECHNOLOGY
Gothenburg, Sweden 2025
www.chalmers.se

Master's Thesis in Mobility Engineering

Flow visualization techniques for full-scale test objects in a wind tunnel

Evaluation of a novel flow visualization technique

CLEMENS STEINKE

Department of Mechanics and Maritime Sciences
Division of Vehicle Engineering and Autonomous Systems
Chalmers University of Technology
Gothenburg, Sweden 2025

Flow visualization techniques for full-scale test objects in a wind tunnel
Evaluation of a novel flow visualization technique
CLEMENS STEINKE

Supervisors: Ananda Subramani Kannan and Kaveh Amiri, Volvo Car Group
Examiner: Simone Sebben, Department of Mechanics and Maritime Sciences

Master's Thesis 2025
Department of Mechanics and Maritime Sciences
Chalmers University of Technology
SE-412 96 Gothenburg
Sweden
Telephone +46 31 772 1000

Cover: Flow visualization with the ProCap measurement system.

Typeset in LaTeX
Gothenburg, Sweden 2025

Flow visualization techniques for full-scale test objects in a wind tunnel
Evaluation of a novel flow visualization technique
CLEMENS STEINKE
Department of Mechanics and Maritime Sciences
Division of Vehicle Engineering and Autonomous Systems
Chalmers University of Technology

Abstract

Accurate flow visualization in wind tunnels is essential for aerodynamic optimization and CFD validation. Traditional qualitative methods such as smoke and tufts offer quick insights but lack quantitative precision. Conversely, techniques like Laser Doppler Anemometry (LDA) and Particle Image Velocimetry (PIV) provide detailed flow measurements but involve complex setups and pose safety concerns due to high-powered lasers. This thesis identifies the ProCap system as a measurement system that bridges this gap by providing qualitative and quantitative information with relatively low complexity. ProCap measurements around a full-scale car in a commercial wind tunnel are compared against an existing pressure-based traverse-gear system and CFD simulations. The findings show that ProCap is not sufficiently accurate or consistent for CFD method validation, but can be a valuable tool when evaluating vehicle designs by identifying separated regions and overall flow topology.

Keywords: CFD, flow visualization, procap, wind tunnel, aerodynamics, qualitative measurements, quantitative measurements.

Preface

This report presents the outcome of my master's thesis project carried out at the Department of Mechanics and Maritime Sciences at Chalmers University of Technology during the spring of 2025. The thesis was concluded in collaboration with Volvo Car Group.

Acknowledgements

First of all, I would like to express my sincere gratitude to my supervisors, Ananda Subramani Kannan and Kaveh Amiri, for their invaluable support and insights throughout the thesis. You always made time for my questions and patiently guided me in the right direction.

I also want to extend my gratitude to my examiner, Simone Sebben, for her continuous feedback and guidance throughout the entire project.

Finally, I want to extend a warm thanks to the whole Aerodynamics Department at Volvo Cars, including the wind tunnel mechanics. Your willingness to answer questions and help during my wind tunnel tests has been of great value. Most of all, thank you for all of the interesting conversations and laughs we have shared beyond the world of aerodynamics. It has been a pleasure to be a part of your team.

Clemens Steinke, Gothenburg, June 2025

List of Acronyms

BEV	Battery Electric Vehicle
CFD	Computational Fluid Dynamics
DDES	Delayed Detached Eddy Simulation
DES	Detached Eddy Simulation
EU	European Union
GIS	Grid Induces Separations
ICE	Internal Combustion Engine
IDDES	Improved Delayed Detached Eddy Simulation
LES	Large Eddy Simulations
LDA	Laser Doppler Anemometry
NEDC	New European Driving Cycle
PIV	Particle Image Velocimetry
RANS	Reynolds-Averaged Navier-Stokes
SUV	Sport Utility Vehicle
TG	Traverse-Gear
PVT	Volvo Cars aerodynamic wind tunnel
WDU	Wheel Drive Unit
WLTP	Worldwide Harmonised Light Vehicles Test Procedure
5hp	5-hole probe
14hp	14-hole probe

Parameters

A	Frontal area
c_D	Drag coefficient
$c_{p,tot}$	Total pressure coefficient
d_w	Wall distance
F_D	Drag force
$\tilde{f}_d$	Shielding function
$f_{restore}$	Restoration function
k	Turbulent kinetic energy
L	Length scale
N	Number of measurement points
P	Pressure
p_{tot}	Total pressure
P_∞	Free-stream static pressure
S	Anti-symmetric component of velocity gradient
S_{ij}	Strain rate tensor
t	Time
t_{95}	Two-tailed Student's distribution
U	Relative velocity
u	Velocity
u'_i	Time-averaged fluctuating velocity component
$\bar{u}_i$	Time-averaged mean velocity component
U_∞	Free-stream velocity
∇u	Velocity gradient
α	Yaw angle
β	Pitch angle
δ_{ij}	Kronecker delta

θ	Flow angle
ν_t	Eddy viscosity
ρ	Density
σ	Standard deviation
σ_{ij}	Viscous stress tensor
τ_w	Wall shear stress
ϕ	Angle around probe axis
Ω	Symmetric component of velocity gradient
ω	Specific dissipation rate

Contents

List of Figures

List of Tables

1

Introduction

1.1 Background

With the European Union (EU) trying to reduce its carbon footprint, stricter targets are being introduced for new passenger cars. Between 2020 and 2024, the target was 95 gCO_2/km for the NEDC driving cycle, which is reduced to 93.6 gCO_2/km for the years 2025-2029. It will further be lowered to 49.5 gCO_2/km for 2030-2034, and finally set to 0 gCO_2/km from 2035 and onward [1]. Achieving these goals will require further improvements in vehicle energy efficiency. While advancements in powertrain technology and the usage of sustainable energy sources are essential, reducing resistive forces such as aerodynamic drag and rolling resistance is equally as critical. At speeds over 80 km/h, the aerodynamic force becomes the largest of the resistive forces, see Figure 1.1, underlining the importance of keeping it to a minimum [2].

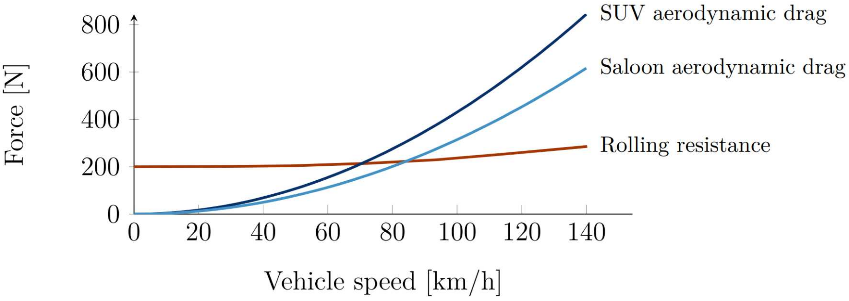

Figure 1.1: Aerodynamic drag compared to rolling resistance for a representative saloon and SUV type car [2].

Modern vehicle aerodynamic development combines wind tunnel testing with computational fluid dynamics (CFD) simulations to address this aerodynamic challenge. Although CFD is usually much cheaper, wind tunnels remain essential because the complex fluid flow equations governing airflow around cars cannot be solved exactly and must be approximated in simulations, introducing some error. Wind tunnel testing provides more accurate global force measurements, such as drag and lift, ensuring reliable validation. Conversely, CFD excels in flow visualization by offering detailed data at every point in the domain, making it easier to identify areas for aerodynamic improvement. Together, these methods complement each other, balancing accuracy and insight in vehicle design.

There are also ways to visualize the airflow in the wind tunnel. The issue is that traditional wind tunnel flow visualization techniques, such as tufts or smoke, only give qualitative indications of the flow, which can be insufficient compared to simulations. While there are established, extensive techniques that provide quantitative data, for example, Laser Doppler Anemometry (LDA), Particle Image Velocimetry (PIV), and hot wire anemometry, they all have their respective drawbacks, making them non-ideal. Thus, a method that combines the accuracy of the quantitative methods and the visualization capabilities of the qualitative methods is needed.

1.2 Objective

There are many well-established flow visualization techniques for wind tunnels, each with its own strengths and limitations. Some are extremely accurate but expensive and time-consuming to use, while others are inexpensive and easy to use but provide limited information about the flow. The aim of this thesis is to identify and investigate a flow visualization method that combines ease of use with the ability to deliver accurate quantitative data. The objectives are summarized as:

- Identifying a measurement system that can bridge the gap between qualitative and quantitative flow visualization techniques.
- Evaluating the identified system to determine its strengths and weaknesses, and positioning it relative to other established methods.
- Investigating if the system is suitable for CFD method validation.

Additionally, the aim of the thesis is to learn more about the operation of aerodynamic development at an automotive company. In particular, how to conclude tests in a large-scale commercial wind tunnel and gain proficiency in using commercial CFD software.

2

Theoretical background

This chapter provides an overview of key concepts in vehicle aerodynamics and introduces parts of the car that are investigated in this thesis from an aerodynamic perspective. Furthermore, the general concepts of a wind tunnel and flow visualization techniques are introduced. Finally, Computational Fluid Dynamics (CFD) and its challenges are discussed.

2.1 Vehicle Aerodynamics

Vehicle aerodynamics is about understanding and optimizing the interaction between a vehicle and the surrounding airflow. This can be done with multiple objectives in mind, such as improving vehicle stability or increasing driving range. With Battery Electric Vehicles (BEV) gaining popularity, aerodynamic efficiency plays an increasingly important role in extending range. Figure 2.1 illustrates how the share of total energy loss to aerodynamic drag increases from around 8% for internal combustion engine (ICE) vehicles to approximately 30% for BEVs. Correspondingly, aerodynamic development is crucial to the energy efficiency gains in any modern BEV. The following sections will introduce relevant vehicle aerodynamics concepts.

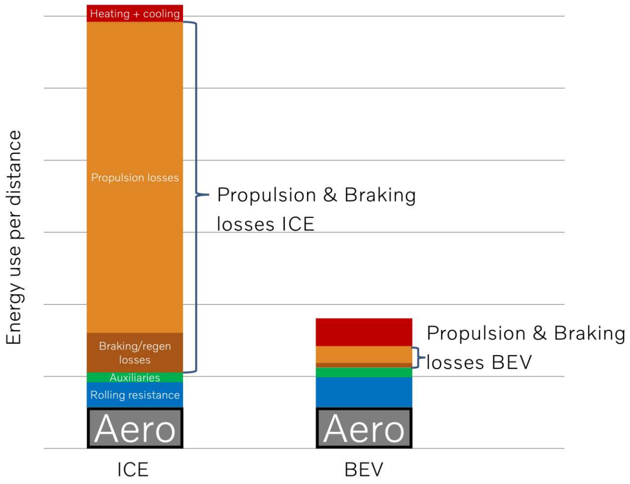

Figure 2.1: Energy used per distance for the standardized WLTP driving cycle from the different attributes for a generic BEV and ICE vehicle [3].

2.1.1 Aerodynamic forces

Placing a bluff body, such as a car, in a flow will affect both the flow and the body itself. The flow's velocity and pressure will change, while the body will experience forces and moments. The forces on the body are split into two types: skin friction and pressure force. The skin friction force is a consequence of the no-slip wall condition, meaning that the flow particle right next to the body has no relative velocity to the body's surface. This creates a velocity gradient from the surface to the free stream velocity, i.e., the boundary layer. The gradient causes shear forces proportional to the velocity gradient and the fluid's viscosity, acting tangentially at the wall.

The pressure force is the result of integrating pressure over the object's surface. Normally, there is a stagnation area with high pressure in the front of the body and a separation with low pressure at the back. This results in a force component along the flow direction, resisting the object's motion relative to the flow. Therefore, a vehicle shape that results in a small stagnation area at the front and a small wake footprint at the rear is preferable to minimize this force. Correspondingly, aerodynamic development is focused on pressure recovery to minimize the differential between the front and rear ends.

The total aerodynamic force acting on a vehicle in the direction of motion is typically expressed in dimensionless form to enable comparison between different aerodynamic shapes. This force component is known as drag, and the corresponding non-dimensional force is represented by the drag coefficient, c_D, defined as:

$$c_D = \frac{F_D}{\frac{1}{2}\rho A U^2} \tag{2.1}$$

where F_D is the drag force, ρ is the density of the fluid, A is the projected frontal area presented in Figure 2.2, and U is the relative velocity between the fluid and the object. Drag can also be expressed in counts, where 1 count = 0.001 c_D [4].

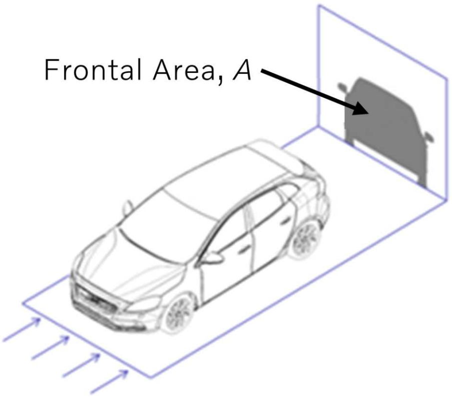

Figure 2.2: Frontal area definition for a road vehicle.

2.1.2 Flow separation and related metrics

Flow separation and backflow can occur when a viscous boundary layer encounters a pressure gradient acting against the flow direction. The reason for this is that the gradient opposes the momentum of the flow, which is already weakened near the surface due to viscosity, eventually overwhelming it and reversing the flow direction [4]. As shown in Figure 2.3, the detachment point is located where

$$\tau_W = \left(\frac{du}{dy}\right)_{wall} = 0 \tag{2.2}$$

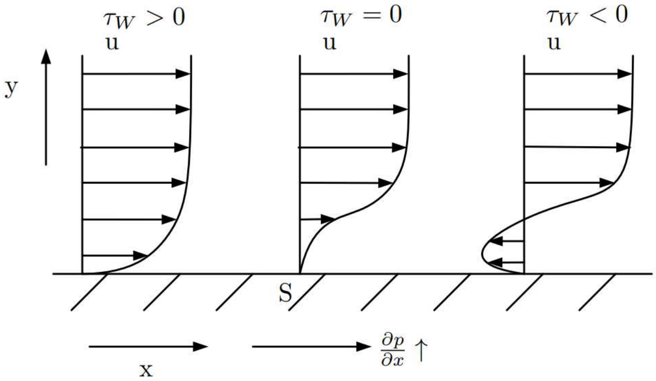

Figure 2.3: The 2D boundary layer velocity profile from attached to detached. The velocity close to the surface decreases until it reaches zero, after which the flow direction gets reversed, resulting in separation [5].

A common way to capture separated areas of flow around bluff bodies is to create an isosurface where the total pressure coefficient, $c_{p,tot}$, is zero. The coefficient is a non-dimensional measure that quantifies how much of the total pressure has been dissipated relative to free-stream conditions. It is defined as

$$\frac{p_{tot} - p_\infty}{\frac{1}{2}\rho U_\infty^2} \tag{2.3}$$

where p_{tot} is the total pressure, p_∞ is the free-stream static pressure, and U_∞ is the free-stream velocity. A $c_{p,tot}$ close to zero indicates significant energy dissipation and is typical in areas with separated flow. To instead portray highly rotational areas of the flow, the Q-criterion can be used. It is based on the idea that a vortex exists in regions where the rotation of the fluid dominates over the strain, or deformation. It is defined as

$$Q = \frac{1}{2}(||\Omega||^2 - ||S||^2) \tag{2.4}$$

with Ω and S being the symmetric and anti-symmetric components, respectively, of the velocity gradient, ∇u [6]. A positive value of Q indicates that local rotation dominates over strain, suggesting the presence of a vortex.

As shown in Figure 2.4, flow separations and rotational, or vertical, structures are created at several regions along the length of a car. The largest separation is at the base wake, located at the rear. A well-balanced and preferably small base wake is crucial to achieve an aerodynamically stable and efficient car [7]. Upstream from the base wake, there are separations coming from both the A and C-pillars. These feed into the base wake and have a significant effect on it. In particular, the highly rotational vortices created by the C-pillar, and to some extent the A-pillar, influence the rotation of the base wake [8]. Another significant separation comes from the side-view mirrors, which can interact with the A-pillar vortex. The wheels also create large separations, with the rotation of the wheels adding additional complexity to the structure and vorticity of the base wake.

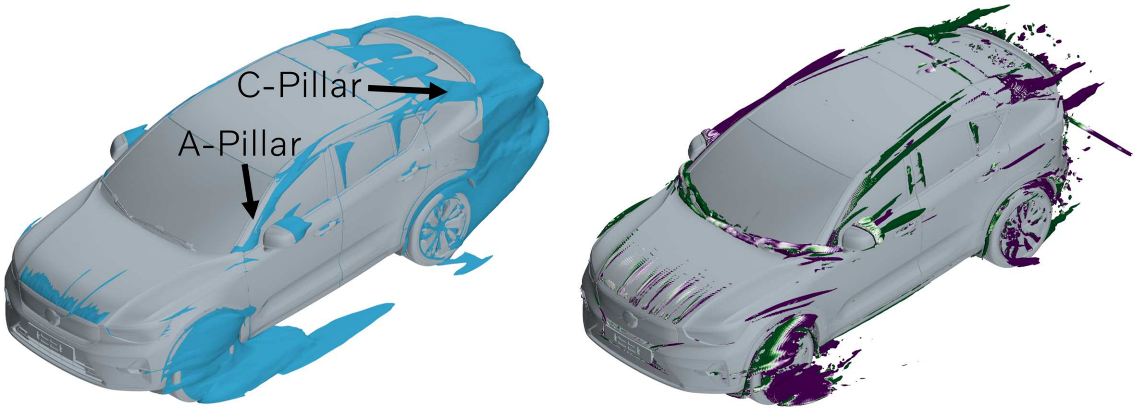

(a) Isosurface of $c_{p,tot} = 0$, showing regions of separated flow

(b) Isosurface of Q-criterion = 10000 s^{-2}, highlighting rotational flow structures

Figure 2.4: Visualization of flow behavior around a Volvo EC40.

The topology and behavior of flow separations around the vehicle body are vital for its aerodynamic performance, underlining the importance of obtaining accurate data about the latter to achieve effective design improvements [5][9].

2.2 Relevant vehicle features

The following sections briefly review vehicle features within the context of this thesis from an aerodynamic perspective. The features are illustrated in Figure 2.5.

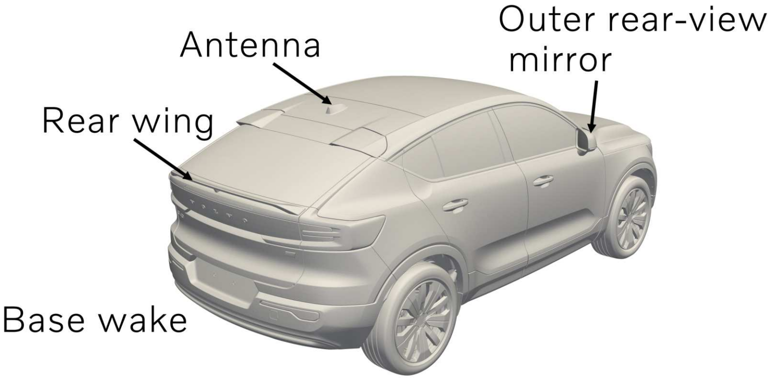

Figure 2.5: Features of the car relevant in this thesis.

2.2.1 Rear wing

The rear wing's main function is to create downforce, which increases the vehicle's grip and consequently stability. To achieve this, the shape of the wing accelerates the flow on its underside, creating a lower pressure compared to the top, resulting in a force component pushing the car into the ground. In addition to creating downforce, the rear wing also exerts a force against the direction of travel, adding drag. Despite this, the overall effect on the car's drag coefficient can be positive as well as negative. For example, [10] shows an increase and [11] shows a decrease in drag when adding a rear wing. The reason for this is that the rear wing can positively affect other areas of the flow, for instance, delaying separation on the rear window and balancing the base wake, reducing the drag [12].

There are multiple other ways a rear wing can enhance a vehicle's performance. In motor racing, where grip is important to corner as fast as possible, it contributes to creating downforce. For a passenger car, a rear wing can help with vehicle stability by improving the lift balance between the front and rear axle, as well as having a stabilizing effect on the base wake [7].

2.2.2 Outer rear-view mirrors

The mirrors provide a greater spatial awareness for the driver without the need to turn the head excessively, and are legally mandated to be included in a passenger car. While adding value in terms of safety, side-view mirrors are usually not good for the aerodynamic performance of a car. It is a bluff body exposed directly to the oncoming airflow, creating drag and flow structures that can interfere with the rest of the car.

From an aerodynamic standpoint, the outer rear-view mirrors need to be optimized in a similar manner to any other bluff body. Just like the car as a whole, the mirrors have a pressure differential between the front and the back, causing the main portion of their drag contribution. Moreover, small changes, such as reducing the gap between the mirror housing and the side window, changing the mirror housing's angle, or reducing the trailing surface curvature, can significantly improve its aerodynamic performance. In total, the side-view mirrors account for around 2-7% of a car's total drag [13].

Developing a mirror purely with CFD can be challenging. While some changes produce clear c_D deltas, others give deltas that are too small for CFD to reliably capture. In those cases, wind tunnel testing becomes especially important [13]. Usually, a combination of CFD and wind tunnel optimizations is performed while developing an outer rear-view mirror.

2.2.3 Antenna

The typical design of a car antenna has changed in recent years from the traditional bee-sting to a shark fin shape, increasing the possibilities for aerodynamic optimization [14]. Despite this, optimizing the antenna can be difficult due to its small size, making CFD simulations unreliable. For instance, solving the flow with two different turbulence models can give conflicting c_D trends. Similar to the mirror, the difficulty of accurately evaluating the aerodynamic performance using CFD highlights the importance of wind tunnel optimization of the same [15].

2.2.4 Base wake

The drag of a car is dominated by the pressure drag caused by the high pressure in the front compared to the low pressure at the rear, accounting for as much as 80% of the total drag [16]. Therefore, reducing this pressure differential is vital for optimizing the aerodynamic performance. The low pressure comes from the flow not being able to follow the sharp corners at the rear of the car, causing a region of separated flow which forms the base wake. The topology of this wake not only has a large effect on the drag, but also on the rear lift. If the wake is pointing in an upward direction, the car will experience negative lift, or downforce, and the opposite is true if the wake points downward. In most cases, striving for a balanced base wake is desirable both in terms of drag and lift [17].

Highly rotational vortex structures from the A/C pillars, mirrors, wheels, etc., often merge into the base wake, adding additional complexities. In the case of a sedan or fastback-type vehicle, as investigated in this work, a significant vortex pair originating from the C-pillar will affect the base wake. Thus, designing the car so that the interaction between these vortices and the base wake works favorably is of great importance for both the drag and stability [18].

2.3 Wind tunnel

Evaluating the aerodynamic performance of a car while driving on a normal road can be difficult and inconvenient. While qualitative measurements with, for example, tufts are possible on a moving car, quantifying the exact forces and moments is hard. An alternative is having the car stand still and having the air and road move past it instead. From the point of view of the car, these two alternatives are equivalent. Due to the more practical nature of having the car standing still, most aerodynamic testing for road vehicles, including that in this thesis, is done in a wind tunnel.

The most fundamental task of a wind tunnel is to provide a controlled and continuous air flow through the test section, normally driven by a fan. There are two main types of wind tunnels, open return and closed return. The open return type continuously draws new air into the tunnel, with only small recirculation, if any. In contrast, a closed return wind tunnel fully reuses the air by circulating it. Both types have advantages and disadvantages compared to each other. Generally, the closed return type has better flow quality and lower operating costs. This is because the fan only needs to compensate for losses in the flow and not accelerate new air continuously, which the open return type does. On the other hand, an open return tunnel is cheaper to construct and does not accumulate smoke or exhaust [19][20].

An inherent problem when having a closed test section is the blockage effect that the walls and roof bring. It significantly affects the flow by compressing the streamlines, resulting in higher velocities and an increased drag coefficient. There are multiple ways of trying to mitigate the blockage effect, the most primitive being to remove the walls and roof (open-jet). However, there will be a significant shear layer buildup between the moving and ambient air, inducing turbulence into the flow that negatively affects the flow quality. A compromise is to have a slotted wall test section, giving a reduced blockage effect without as much turbulence from the shear layer buildup [21][22].

An important feature of modern road vehicle wind tunnels is that they emulate wheel rotation and ground movement relative to the car, usually with the same speed as the wind. If this is to be neglected, the flow around the test object will not replicate the flow at actual driving conditions. The reason for this is that a boundary layer will grow between the fixed ground and the free stream velocity, which will interfere with the rest of the flow. There are different ways, often used in combination, to solve this problem. The most intuitive solution is to have a moving belt system. Even though it resembles a moving ground very well, there are challenges associated with such a system. For instance, the test object needs to be held in place to minimize movement and vibrations. There are multiple methods to achieve this, for example, mounting the object with struts or having a large sting holding it. While these devices have different strengths and weaknesses, they have one problem in common: they disturb the flow [23].

Considering it is not feasible for the moving belt to span the entire tunnel, additional methods are needed to minimize the boundary layer prior to the moving belt. One method is to use a boundary layer scoop, which removes the boundary layer by channeling away the flow close to the ground. Another method is having suction through a porous ground floor to minimize the thickness of the boundary layer. Finally, a high-velocity jet can be deployed close to the ground to energize the boundary layer, referred to as tangential blowing. While these methods all have their own strengths and weaknesses, they can be combined to mitigate these and create a robust boundary layer control system [24] [25].

2.4 Flow measurement and visualization techniques

Wind tunnels not only offer accurate force measurements but can also provide highly valuable information about the flow topology around the test object. This information can be crucial for further optimizing designs. Since airflow is not visible to the naked eye, measurement or visualization techniques are needed to reveal its behavior. The subsequent sections present the most commonly used methods.

2.4.1 Smoke

The fundamental principle of this technique is to visualize the flow by injecting smoke into it. There are multiple ways of introducing the smoke into the flow, many being highly flexible, reaching areas of the test body that can be hard to access with more sophisticated methods. The smoke can, for example, be injected using a rod, grid, or even through the surface of the test body. This flexibility comes with the cost of disturbing the flow. For instance, when a person holds the injection rod, their presence affects the flow, which can cause unwanted interactions with the flow field around the test object. To minimize these effects, careful placement of the smoke equipment and its operator is important. Figure 2.6 shows smoke visualization used to showcase the airflow around a car.

Figure 2.6: Smoke visualization in the Volvo Cars wind tunnel for a touring car [26].

There are multiple ways of producing the smoke, for example, burning light oils or using chemical reactions to create the smoke. Chemicals used for this purpose are titanium tetrachloride and tin tetrachloride, among others [27]. An issue with the smoke produced is that it can be corrosive and toxic. For example, using anhydrous ammonia produces sulfuric acid, which has both of these unwanted properties [28]. Another issue is that the smoke ideally should have a neutral buoyancy and a low mixing rate with the main flow. This is not the case for smoke, making it difficult or impossible to use smoke in highly turbulent areas with high mixing rates, for instance, close to rotating wheels. Despite these shortcomings, smoke can give a rapid qualitative perception of the flow, especially for visualization of vortices and flow separation. Furthermore, the technique is relatively cheap and easy to use, making it a popular and well-used technique in the industry.

2.4.2 Surface oil films

Surface oil films are used to visualize the flow close to the surface of an object. The technique involves applying an oil mixed with dissolved pigments to the surface before exposing it to the airflow. The oil will partly get smeared out by the shear forces from the flow, leaving a streaky pattern indicating the flow topology, as shown in Figure 2.7. While this method is mainly qualitative, it is possible to estimate the wall shear stress by measuring the variation in film thickness [29].

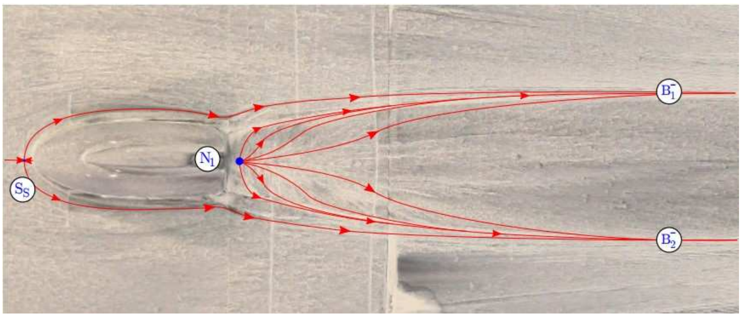

Figure 2.7: Surface oil applied around a car antenna, indicating the flow topology. S_S indicates a saddle point, N_1 a node point of attachment, and B_1^-, B_2^- bifurcation lines [5].

Despite this method being theoretically intrusive, its impact on the boundary layer is generally minimal. While oil streaks accurately depict surface streamlines, they tend to indicate flow separation prematurely and should therefore be interpreted carefully. Another issue with surface oil is that it can contaminate the wind tunnel if it detaches from the surface, which can require time-consuming cleaning jobs [30]. Detailed analysis of the streak patterns is also required, which further adds to the time aspect. In general, surface oil can provide valuable insight into surface flow behavior, but it is often time-intensive due to the necessary preparation, cleaning, and data interpretation.

2.4.3 Tufts

A tuft is a short string attached to the test object that can give a perception of the flow with its movement. In addition to showing the flow direction, it can also indicate the flow type. For laminar flows, the tuft will stay almost perfectly still, while for a more turbulent boundary layer, the tuft oscillates in a controlled manner. If the flow is detached and recirculating, the tuft will exhibit erratic and unstable movements. By placing multiple tufts on the vehicle surface, observers can visually identify points of flow separation. This information is essential for understanding the aerodynamic behavior of the vehicle and plays a critical role in optimizing its design. Figure 2.8 shows tufts attached to a helicopter.

Figure 2.8: Tufts used to visualize airflow around a helicopter [31].

Similarly to using smoke for visualization, tufts have the problem of being intrusive. Both the tufts themselves and their fasteners may create small separations that can affect the flow. Considering that the method is traditionally purely qualitative, these small disturbances might not play a large role. However, there have been recent attempts to obtain quantitative information on the flow by tracking the tufts with computer vision. In that case, the disturbance created could become of greater importance [32][33]. Due to the simplicity and affordability of the tuft, they are widely used in the aerodynamic industry. With further research into the incorporation of a quantitative aspect, the technique could become even more valuable in the future.

2.4.4 Hot wire anemometry

Hot-wire anemometry is a measurement technique that quantitatively determines the velocity of a fluid at a single point. A typical 1D hot wire probe has two arms that are connected via a thin metal wire. The wire is heated by a current, while the fluid flowing past it cools it. Using the fact that the wire has a changing resistance with temperature, there are two main ways to determine the flow velocity. The first is to pass a constant current through the wire and measure the resistance with a Wheatstone bridge. A relationship can then be formed to obtain the fluid velocity from the resistance of the wire (Constant Current Anemometry). The second option is to keep the temperature of the wire constant and measure the current, which can also be calibrated to provide the fluid velocity (Constant Temperature Anemometry). The latter is a more common operating mode than the former. Although one wire can only measure one velocity component, using multiple wires can give velocity components for more than one direction [34].

The main strength of hot-wire probes is that they have a very high-frequency response, which makes them suitable for studying highly turbulent and unsteady flows. They also have a high spatial resolution and can be made very small, which limits their intrusiveness. On the other hand, hot-wire probes' main weakness is that they are very fragile and can not handle contamination well. They can also be inaccurate when measuring very slow flows due to the wire's natural convection [35].

2.4.5 Particle Image Velocimetry

Particle Image Velocimetry (PIV) is a measurement technique for extracting quantitative velocity data from a flow field. Despite being a relatively modern technique, visualizing a flow by scattering small particles into it is not new [36]. In fact, Ludwig Prantl already used this technique in the early 1900s. Back then, only qualitative, of course. With developments in camera and computer technology, today it is also possible to retain quantitative data [37].

The principle of PIV is to use a pulsating laser to form a sheet to illuminate particles that are seeded into the flow. The particles can be gaseous, liquid, or solid. It is essential that the particles are small enough not to interfere with the flow, but still large enough to be captured by a camera. Even more importantly, the particle inertia should be low to be able to follow the flow accurately. With each laser pulse, a high-speed camera records the particles. Since the time step between pulses is known, the velocity can be easily calculated from the movement of each particle [38]. Figure 2.9 illustrates the principal setup of a PIV system.

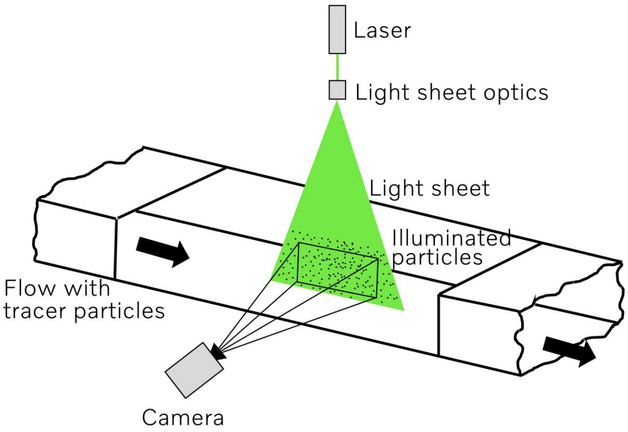

Figure 2.9: Schematic of a basic PIV setup. Adapted from [39].

The tracing of particles can be very accurate, normally around 0.1 pixel, which can give accuracies of 0.5-5% depending on the measurement conditions [40][41][42]. Depending on the laser setup, the technique can also be non-intrusive. On the other hand, the equipment is expensive, can have a long setup and post-processing time, and can be dangerous for operators due to the strong laser [43][38].

2.4.6 Laser Doppler Anemometry

Similar to PIV, Laser Doppler Anemometry (LDA) is a measuring technique using lasers and scattered particles to determine the velocity of the flow. The main difference between the methods is that LDA measures the velocity at a single point in space, not a plane or volume, as done with PIV. LDA uses a laser beam, split into two parts, passing through a lens that bends them into a focal point. A fringe pattern is established at the focus point where the two beams intersect. When a particle passes through the fringe pattern, it scatters the light, which a photodetector records, as illustrated in Figure 2.10. The scattering of the light contains all the information needed to determine the velocity of the particle.

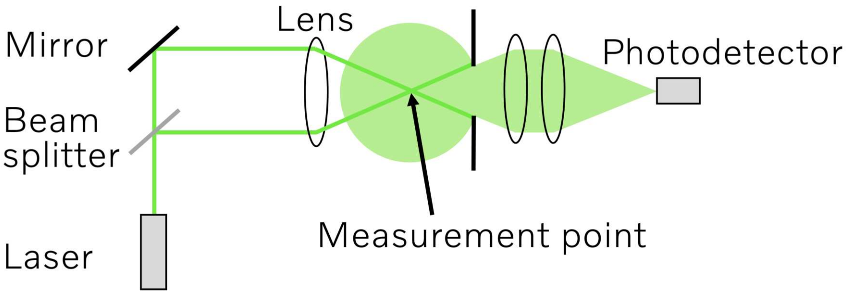

Figure 2.10: A principal LDA setup to measure velocity in a single point. Adapted from [44].

The main strength of LDA lies in its non-ambiguous approach to determining the velocity, resulting in very precise measurements. In fact, LDA is the most accurate measurement technique presented in this thesis, with an accuracy usually well below 1% [45][46]. Another strength is its ability to determine velocity components in a normal direction very close to surfaces, which can be difficult with other techniques, such as hot wire anemometry. A disadvantage of the technique is that it measures the velocity of the scattered particles and not the flow itself. If the particles follow the flow well, that is not an issue. However, the measurements do not give accurate results if the particles are too large and deviate from the flow velocity [47]. Furthermore, as for PIV, handling lasers can be dangerous, making the technique difficult and time-consuming to use.

2.4.7 Pressure-based velocity measurements

While pressure readings can give interesting information about a flow by themselves, they can also be used to calculate velocity. In 1732, Henri Pitot used this to invent the Pitot-static tube, a tool giving velocity readings from pressure measurements. Despite its early discovery, it is still widely used today, for example, in measuring wind speed for airplanes and ducts [48]. Pitot-static tubes work by measuring the difference between the total and static pressure. The total pressure is measured at the stagnation point at the probe's tip, where the velocity is zero. The static pressure is measured through a hole tangential to the flow, generally at the side of the tube. Based on the Bernoulli equation, the static pressure p_∞ and total pressure p_{tot} are related to the free stream velocity U_∞ as follows:

$$p_{tot} = p_\infty + \rho \frac{U_\infty^2}{2} \tag{2.5}$$

Rearranging and solving for the velocity gives

$$U_\infty = K \sqrt{\frac{2(p_{tot} - p_\infty)}{\rho}} \tag{2.6}$$

where K is a correction factor for the deviation from the Bernoulli equation [49]. The accuracy of Pitot-static probes can be an issue, with an error of around ±5%, but more expensive probes with around ±1% error exist. Although this method is intrusive, depending on the size of the probe, the impact on the flow can be small.

For the probe to work correctly, it must be pointed in the direction of the flow, which is not always easy to achieve. To avoid having to do so, probes with multiple holes at the tip can be used, known as multi-hole probes. Not only are they more versatile by not requiring the tip to be pointed precisely into the flow, but they can also compute all three velocity components and simultaneously give the static pressure. An illustration of a typical 5-hole probe is shown in Figure 2.11. It shows the port numbering, P_i, with $i = 1, 2, 3, 4, 5$, as well as the definition of the yaw angle, α, and pitch angle β. The rotation around the probe axis is denoted by ϕ and the flow angle by θ.

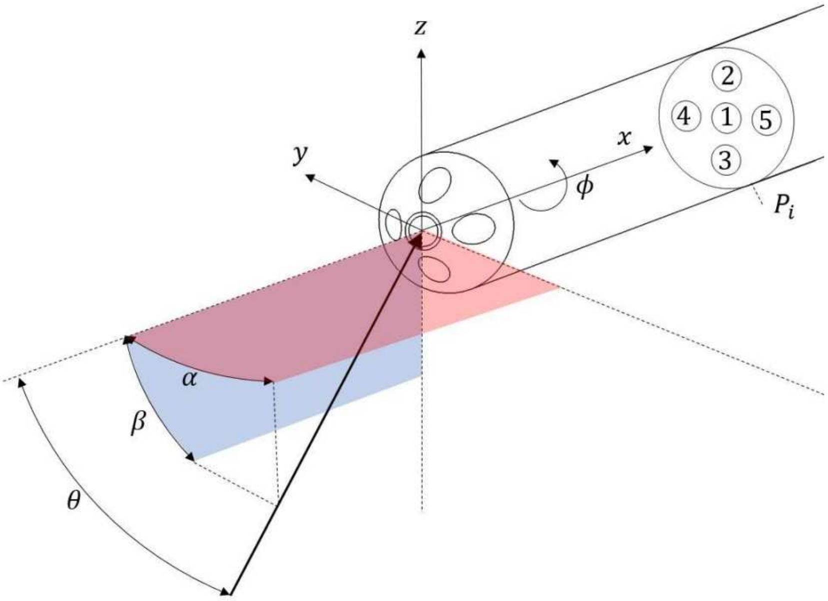

Figure 2.11: A schematic of a typical 5-hole probe [50].

In contrast to Pitot-static probes, multihole probes do not employ the Bernoulli equation directly. Instead, they either convert pressure readings to calibration coefficients and then apply the Bernoulli equation, or employ a calibration map to extract the velocity straight away. The calibration coefficients, or map, come from a calibration procedure where the pressures are recorded for a variety of known flow angles and velocities [50].

While multihole probes are intrusive by nature, a significant amount of their intrusiveness can be calibrated out. However, the intrusive effects of multihole probes still need to be taken into consideration, especially if they are held in place by an intrusive object [51]. Multihole probes are generally accurate to around 1% or 1 m/s, whichever is greater [52].

2.5 Computational Fluid Dynamics

Instead of performing wind tunnel tests to evaluate a vehicle's aerodynamic performance, an option is to simulate the flow with Computational Fluid Dynamics (CFD). This method overcomes the limitations of wind tunnels in terms of flow visualization. Quantities can be interpolated to any point in the domain, making the visualization opportunities nearly infinite.

2.5.1 Governing equations

The equations for simulating fluid flow are derived using the law of mass conservation and Newton's second law, resulting in the continuity and momentum equations. Together, these equations are called the Navier-Stokes equations. For a compressible, unsteady, and viscous flow, they are stated as follows:

$$\frac{\partial \rho}{\partial t} + \frac{\partial (\rho u_j)}{\partial x_j} = 0 \tag{2.7}$$

$$\frac{\partial (\rho u_i)}{\partial t} + \frac{\partial (\rho u_i u_j)}{\partial x_j} = -\frac{\partial P}{\partial x_i} + \frac{\partial \sigma_{ij}}{\partial x_j} \tag{2.8}$$

where u_i is the velocity and x_i the position in the ith component, with $i = 1, 2, 3$. The density is ρ, μ is the viscosity, and P is the pressure. The viscous stress tensor, σ_{ij}, is defined as

$$\sigma_{ij} = \mu \left(2S_{ij} - \frac{2}{3} S_{mm} \delta_{ij} \right) \tag{2.9}$$

In this form, the term $-\frac{2}{3}\mu S_{mm}\delta_{ij}$ represents the contribution of the volumetric strain rate to the normal viscous stresses with δ_{ij} being the Kronecker delta and S_{ij} being the strain rate tensor. The repeated index m implies summation over that index (Einstein summation convention). Therefore,

$$S_{mm} = S_{11} + S_{22} + S_{33} = \frac{\partial u}{\partial x} + \frac{\partial v}{\partial y} + \frac{\partial w}{\partial z}.$$

This sum is the divergence of the velocity field ($\nabla \cdot \mathbf{v}$) and represents the volumetric strain rate or the rate at which the volume of a fluid element is changing per unit volume. A positive S_{mm} indicates expansion, while a negative S_{mm} indicates compression. For an incompressible flow, $S_{mm} = 0$.

The strain rate tensor S_{ij} that describes the rate at which a fluid element is deforming is defined as:

$$S_{ij} = \frac{1}{2} \left(\frac{\partial u_i}{\partial x_j} + \frac{\partial u_j}{\partial x_i} \right) \tag{2.10}$$

While the Navier-Stokes equations can be solved analytically for very simple cases, it is not possible to do so for complex geometries such as cars. For such cases, the equations need to be discretized, and an iterative solver must handle their non-linear and coupled nature. The issue with discretizing is that it introduces an error. Therefore, it is important to remember that CFD simulations are approximations of the flow and not exact [53].

2.5.2 Turbulence modeling

The behavior of a flow can be categorized as laminar or turbulent. Laminar flow flows smoothly and does not have velocity fluctuation, while turbulent flow has chaotic, 3-dimensional fluctuations. The flow around cars is normally assumed to be in the turbulent regime, which necessitates the application of appropriate turbulence models [8].

Turbulence manifests visually as eddies within the flow field and contributes to the overall chaotic and unpredictable nature of turbulent motion. These eddies vary in size from large scales down to the smallest eddies being around 0.1-10 mm [55]. The energy cascades from large to small eddies until the smallest scales dissipate the energy as heat into the flow.

In theory, the Navier-Stokes equations can solve all turbulence scales, but a mesh that can capture even the smallest length scales of the eddies is required. Using such a mesh would be extremely expensive and infeasible from a computational point of view for most applications [56]. Consequently, several modeling philosophies have emerged to approximate the eddies' influence on the mean flow. A common strategy involves the Reynolds-averaged Navier-Stokes (RANS) equations, which model the time-averaged flow behavior.

Specifically, the RANS equations differ from the original Navier-Stokes equations by decomposing the pressure and each velocity component into a time-averaged and a fluctuating component. This models the statistical effects of turbulence without explicitly resolving the instantaneous eddy motions. Doing so gives an extra term to the equation, the Reynolds stresses, creating a closure problem. It means that the introduction of new unknown fluctuating terms outnumbers the governing equations, preventing a direct analytical solution. To address the closure problem, a common simplification used is the Boussinesq approximation, which proposes modeling the Reynolds stresses as an analogous shear stress

$$-\overline{u_i'u_j'} = \nu_t 2S_{ij} - \frac{2}{3}k\delta_{ij} \tag{2.11}$$

where $\overline{u_i'u_j'}$ are the Reynolds stresses, u_i', u_j' are the time-averaged fluctuating parts of the velocity, and $\bar{u}_i$, $\bar{u}_j$ are the mean velocity parts. The turbulent kinetic energy is denoted by k, and ν_t is the eddy viscosity. After applying this approximation, it is a question of modeling k and ν_t to solve the flow, which can be done in multiple ways [53].

One common approach to turbulence modeling, aiming to provide closure for the RANS equations, is the k-ω SST model. This model operates by introducing two transport equations, one for the turbulent kinetic energy (k) and another for the specific dissipation rate (ω), which is related to the rate at which turbulent kinetic energy is dissipated.

$$\nu_t = \frac{k}{\omega} \tag{2.12}$$

$$L_{RANS} = \frac{\sqrt{k}}{\beta^* \omega} \tag{2.13}$$

with L_{RANS} being the length scale and β^* a model constant [57].

Modeling the turbulence behavior for all scales using RANS is computationally very cheap compared to DNS. For that reason, it has been used almost exclusively in the industry for a long time. However, RANS models provide only a time-averaged representation, thus lacking the resolution necessary to accurately depict important flow structures. Therefore, other methods that resolve the larger turbulent scales have become increasingly more popular. Large Eddy Simulations (LES) is one such method that works by applying a spatial low-pass filter, where eddy scales larger than the filter width are resolved and smaller eddy scales are modeled [58].

It can be tempting to only use LES, but this is also problematic because it would require an extremely fine mesh at the boundary. Therefore, using both RANS and LES can be a good idea. The Detached Eddy Simulation (DES) model does so by applying RANS on near-wall attached flow and LES everywhere else. The following length scales are then used:

$$L_{RANS} = d_w \tag{2.14}$$

$$L_{LES} = C_{DES}\Delta \tag{2.15}$$

$$L_{DES} = \min(L_{RANS}, L_{LES}) \tag{2.16}$$

where d_w is the normal distance from the wall, $C_{DES} \approx 0.65$ is an empirical constant, and Δ is the grid length scale. An issue that arises with this method is that it can switch to LES prematurely if the grid spacing is too fine, causing the flow to separate early, known as Grid Induced Separation (GIS). To avoid this, Delayed Detached Eddy Simulation (DDES) uses a shielding function, $\tilde{f}_d$:

$$L_{DDES} = L_{RANS} - \tilde{f}_d \cdot \max(0, L_{RANS} - C_{DES}\Delta) \tag{2.17}$$

This delays the transition to LES and thereby shields it from GIS [57].

In the transition regions between RANS and LES, often termed "grey areas", inconsistencies can arise in their respective turbulence production mechanisms. This can lead to an underpredicted amount of turbulence due to suppressed eddy viscosity, which can delay separation. To counteract the damping of the eddy viscosity, a restoration function, $f_{restore}$, is applied to the DDES method, resulting in the Improved Delayed Detached Eddy Simulation (IDDES) method:

$$L_{IDDES} = \tilde{f}_d(1 + f_{restore})L_{RANS} + (1 - \tilde{f}_d)L_{LES} \tag{2.18}$$

The restoration term boosts the RANS length scale in the grey area, helping to better match the turbulence characteristics between RANS and LES [57]. A conceptual illustration of the usage of RANS and LES in IDDES is shown in Figure 2.12.

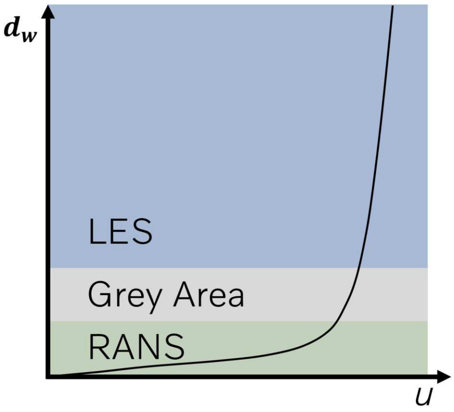

Figure 2.12: A schematic representation of the areas of usage for RANS and LES, including the grey area where the restoration function, $f_{restore}$, is active. The mean velocity and wall distance are denoted by u and d_w, respectively.

In summary, addressing the complex turbulent flow around vehicles in CFD necessitates a spectrum of methods, from computationally intensive DNS to efficient RANS. In between, LES offers higher accuracy by resolving larger eddies and modeling smaller ones, but remains costly for full vehicles. Importantly, hybrid RANS-LES methods like DES, DDES, and IDDES balance cost and accuracy for complex automotive flows with separation, blending RANS near walls with LES in wakes. Their effectiveness is influenced by the underlying RANS model, time step size, and their ability to handle challenges like RANS-LES interface issues [57]. Thus, hybrid methods are key for automotive CFD, with IDDES chosen in this thesis for its balance of cost and accuracy.

3

Methods

The following sections introduce the test object and wind tunnel used, which form the basis for all measurements. Furthermore, the employed measurement systems and the numerical simulation setup are described. Finally, the structure and methodologies for the measurements that were conducted are presented.

3.1 Test object

The test object used in this thesis is a Volvo EC40. It was chosen for its relevant aerodynamic features, such as the rear wing and roof spoiler. The Volvo EC40, together with the corresponding vehicle coordinate system used for visualization techniques and force measurements, is shown in Figure 3.1.

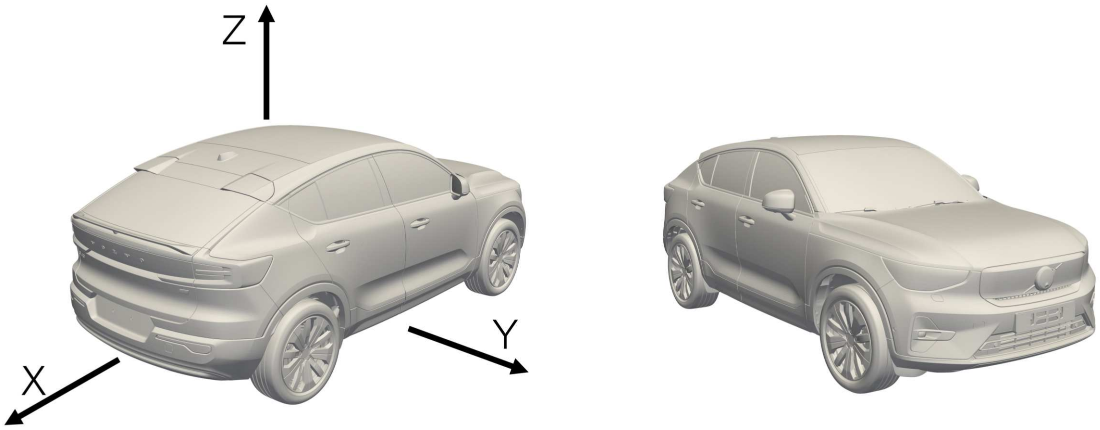

Figure 3.1: Front and rear iso view of the Volvo EC40, including the coordinate system used.

3.2 Volvo Cars Aerodynamic Wind Tunnel

The wind tunnel used in this thesis is the Volvo Cars aerodynamic wind tunnel (PVT), located in Gothenburg, Sweden. It was built in the 1980s, with significant upgrades finished in 2007. The wind tunnel is a closed return tunnel, Göttinger building type, with a 6.6 m wide and 4.1 m tall test section (27.06 m^2). The walls in the test section are slotted with 30% open-area to reduce the blockage effects. A 5 MW fan drives the airflow and can give speeds up to 250 km/h in the test section. The test object is placed on a full-width turn table, capable of rotating ±30°, and held in place with four struts connected to the balance. The balance measuring the forces has an uncertainty of $c_D = \pm 0.003$ if re-mounting the car, and a delta of $\Delta c_D < \pm 0.001$ between repeated measurements without re-mounting the car [5].

With the upgrades from 2007, the test section has an elaborate boundary layer control system consisting of a boundary layer scoop, distributed suction, five moving belts, and tangential blowing [25]. Except for the tangential blowing, all of the mentioned boundary layer control systems were used for this thesis. The boundary layer control system was used to reduce the boundary layer buildup, which can significantly affect the flow structures around the vehicle. To mount the test vehicle, it was connected to the balance via four struts and 360 mm wide wheel drive units (WDU) for each wheel. The layout of the Volvo Cars aerodynamic wind tunnel is illustrated in Figure 3.2.

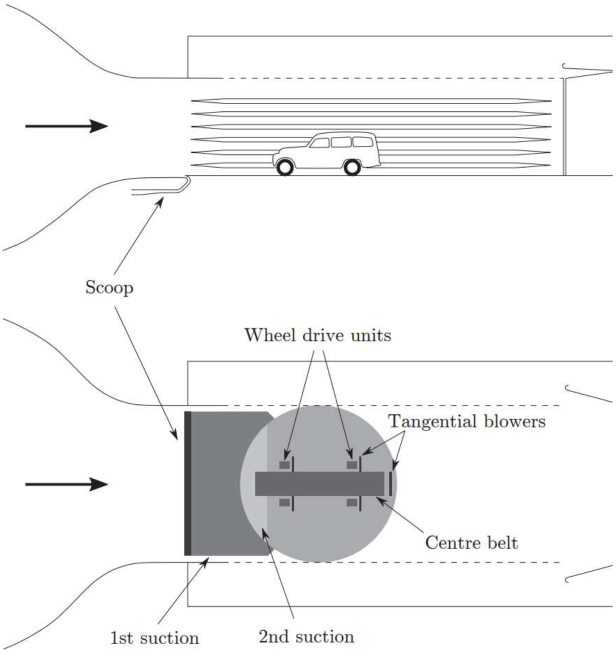

Figure 3.2: Schematic of the Volvo Cars aerodynamic wind tunnel test section with its slotted walls and moving ground system [59].

3.3 Measurement systems setup

The traditional visualization methods all have their advantages and disadvantages, as presented in Chapter 2. The general trend is that the more quantitative and precise the measurement is, the more expensive and time-consuming it gets. A novel pressure-based measurement system, the ProCap measurement system, aims to break this trend by giving accurate quantitative data, without the traditionally expected high effort, see Figure 3.3. The primary objective of this thesis is to evaluate the system for full-scale vehicle aerodynamic investigations.

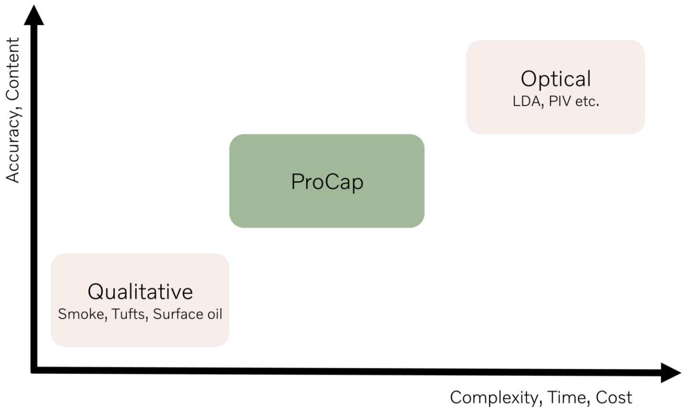

Figure 3.3: Traditional measurement techniques in comparison with the claims of the ProCap system.

Correspondingly, a well-documented traverse-gear-mounted pressure probe (TG) and CFD simulations are used to evaluate the ProCap system and compare its performance to well-established flow measurement techniques. The following sections will describe the ProCap system and how it is used, as well as introduce the traverse-gear system and CFD methodology employed.

3.3.1 ProCap measurement system

ProCap, short for Probe Capture, is a multi-hole pressure probe system designed to provide a flexible and efficient way of obtaining qualitative and quantitative information about a flow. Its core principle is to combine the flow quantities recorded from the pressure probe with positional data recorded via a camera tracking system. This results in a live visualization of the flow in the ProCap Professional software, resembling visualization from flow simulations (CFD).

3.3.1.1 System architecture

Each ProCap measurement is performed by sweeping the probe either by hand or with a traverse system through a user-defined domain, which is discretized into a voxel mesh. A voxel is a 3D pixel that stores all measurements taken while the probe tip is inside it, analogous to a finite volume cell in CFD. The values within each voxel are averaged, and interpolation is applied between voxel centroids to produce a smooth visual representation of the flow.

To ensure data quality, the ProCap system uses a convergence criterion based on the 95% confidence interval, which is calculated as:

$$\mathrm{ConfInt}_u = t_{95}\frac{\sigma(|u|)}{\sqrt{N}} \tag{3.1}$$

where σ is the standard deviation, t_{95} is the two-tailed Student's distribution, N the number of measurement points, and u the velocity. By monitoring the confidence interval, the operator can achieve the desired data quality.

The ProCap system supports a wide range of pressure probes, for example, a 5-hole, a 14-hole, and an ultrasonic probe. In this work, both the 5 and 14-hole probes were used. The 5-hole probe (5hp) is calibrated for velocities between 6-20 m/s, while the 14-hole probe's (14hp) range is 20-64 m/s. Except for the different velocity ranges, the main difference between the probes is that the 14-hole omniprobe has a flow acceptance angle of ±160°, while the 5-hole probe is limited to flow angles below ±60°.

To measure the pressure, each hole at the probe tip is connected to its own differential pressure sensor. The reference pressure used for these sensors is measured from an additional hole at the bottom of the probe, next to the LEMO connection port. All probes, including the 14-hole probe, have three reflective balls mounted in an "L" shape that make it possible for the camera system to detect its position. The complete geometry of the probes is shown in Figure 3.4.

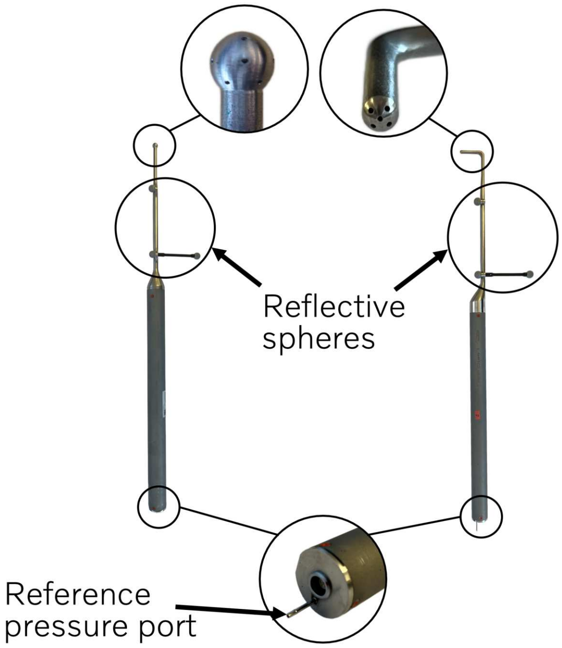

Figure 3.4: The 14-hole omniprobe (left) and the 5-hole probe (right).

The tip of the 14hp is a 7.5 mm sphere, connected via a 5 mm rod to the probe handle where the pressure block is placed. The tip of the 5hp has a diameter of 4 mm, with one hole in the middle and the remaining holes placed around it in a square.

Both probes have a calibration map converting pressures to velocity. The map is created during a calibration procedure, consisting of recording pressures for a range of different flow angles and Mach numbers. These calibration points are used to define the calibration coefficients C_{p_α}, C_{p_β}, C_{p_s}, and $C_{p_{tot}}$. A curve fit is applied to create a relationship between the calibration coefficients and the flow quantities. To mitigate flow separation at the probe tip, which would affect measurements, the tip is segmented into sectors, allowing data acquisition only from holes where flow is likely attached. As a result, the calibration coefficients vary between sectors but are generally defined as

$$C_{p_\alpha} = \frac{p_{n1} - p_{n2}}{D} \tag{3.2}$$

$$C_{p_\beta} = \frac{p_{n3} - p_{n4}}{D} \tag{3.3}$$

$$C_{p_s} = \frac{p_{n5} - p_{n6}}{D} \tag{3.4}$$

$$C_{p_{tot}} = \frac{p_{n7} - p_{n8}}{D} \tag{3.5}$$

$$D = p_{n9} - \frac{1}{N-1}\left(\sum_{i=1}^{N}(p_i) - p_{n9}\right) \tag{3.6}$$

Where $n1...n9$ are strategically chosen port indices, different for every sector, and N is the total number of ports. After the calibration, the 14hp and the 5hp have 2σ standard deviations of 0.41 m/s and 0.16 m/s, respectively.

The tracking system uses an OptiTrack V120 Trio camera, which consists of three infrared cameras with a resolution of 640×480 pixels, a frame rate of up to 120 fps, and a maximum tracking range of approximately 5.2 m. Two of the cameras are equipped with IR LEDs that illuminate the probe's reflective spheres using light at a wavelength of 850 nm. A calibration target is included to calibrate the camera's coordinate system to ensure accurate probe position measurement. Figure 3.5 shows the camera and calibration target.

(a) The OptiTrack V120 trio camera

(b) The calibration target

Figure 3.5: The two components of the optical tracking system.

3.3.1.2 Previous research with ProCap

Given ProCap's recent introduction in 2018, the available published research concerning its application is currently limited. Within the specific context of road vehicle aerodynamics, the literature review revealed a lack of studies concerning the validation of the ProCap system for full-scale production vehicles. Despite the sparse literature, a few articles investigate the validity of the system for different scenarios.

Müller [60] investigates the airflow behind an Ahmed body and a sailing yacht, using the ProCap system and a traverse-mounted pressure probe. It was shown that while giving comparable results in measurement quality with the traverse, the ProCap system was up to a factor of 20 faster overall. Regarding the tracking accuracy, Müller concluded that for a working distance of around 2 m, the tracking was accurate within 1.9 mm and 1.9°.

In a work by Bartl [61], a full wake is analyzed for a yawed model-scale wind turbine. A comparison between results from ProCap and LDA showed good agreement between the two techniques. Bartl showed that highly rotational flow structures generated from the turbine were accurately captured by the ProCap system. Regarding the efficiency of the ProCap system, the study noted a potential for shortening the total measurement time by a factor of 30.

A comparison between CFD simulations and ProCap is concluded by Rembold [62], measuring the flow around a 1:4 scale model car with rotating wheels. Several differences between the two methods were discussed. For example, one area of difference was the boundary layer, which was thicker from the ProCap measurements than from CFD simulations. According to Rembold, this could be because the CFD simulation uses turbulence models that under-predict the boundary layer thickness. Additionally, the velocity near the surface did not drop to zero in the ProCap data. The author argues that this is because of the physical dimensions of the probe, where the velocities cannot be measured closer to the object than the thickness of the probe tip. A final difference mentioned was that the ProCap measurements gave lower velocities under the car, likely coming from the boundary layer build-up in the physical wind tunnel.

In a separate study, Rembold [63] investigated the differences between ProCap and CFD by analyzing the flow around a Formula Student race car. While the overall flow patterns look similar, the main differences lie in the positioning of the vortex cores and the size of the low-pressure zones. It is mentioned that these differences can come from real-world effects that are not captured by the CFD simulations.

3.3.1.3 Measurement procedure

The following procedure was conducted for each ProCap measurement, aiming to collect high-quality data efficiently. The flowchart in Figure 3.6 summarizes the process.

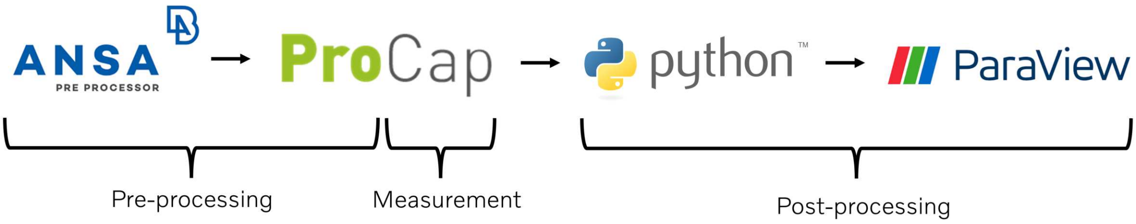

Figure 3.6: Flowchart outlining the software used during the different stages of the ProCap measurement process.

First, the origin of the car's CAD model was moved to an easily identifiable feature on the car using the Ansa pre-processor. In a later step, this reference point was used to align the camera's coordinate system with the ProCap software's coordinate system. The features used on the car for this were an edge on the side view mirror, an edge on the rear wing's center support, and the rear wheel base center, see Figure 3.7. The reference point closest to the measurement area was selected for each measurement.

Figure 3.7: Reference origins, marked in red, used to align the coordinate systems of the CAD model and the camera.

The CAD file with the adjusted origin was then imported into the ProCap software. Its primary purpose was to give the operator visual feedback on the positioning of the probe in relation to the car. If set up properly, the operator could almost exclusively rely on the feedback from the software, minimizing the need to look at the probe itself. The probe, car, and collected data were all displayed simultaneously through the software, significantly streamlining the scanning process.

Next, the measurement domain was defined. Measurement data is only collected while the probe is inside the domain, so it should enclose the complete volume of interest. After defining the domain, it was filled with a voxel mesh. Similar to a CFD mesh, a voxel mesh discretizes the domain. Each voxel, shaped like a cube, stores the measurement data for when the probe was inside it and averages it. The voxel size is defined as the edge length and is set by the user. A voxel mesh for the outer rear-view mirror with a voxel size of 20 mm is shown in Figure 3.8.

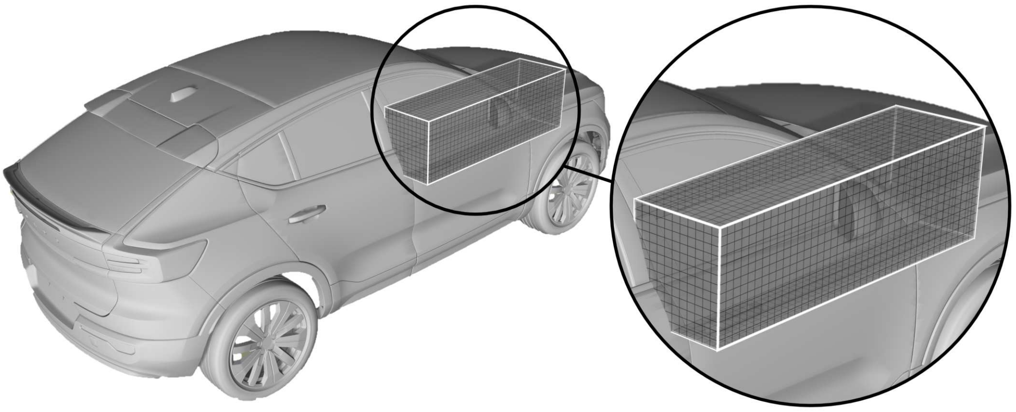

Figure 3.8: Voxel mesh created around the outer rear-view mirror with the ProCap software.

After creating the voxel mesh, planes were defined in the ProCap software. Different methods were used depending on whether a measurement aimed to scan a volume or if only predefined planes were of interest. If a volume was scanned, for example, the mirror wake, planes were defined in a grid filling up the region of interest, as shown in Figure 3.9. Since the probe tip cannot perfectly track a single plane during scanning and tends to oscillate slightly around it, tightly stacked planes ensured good data coverage throughout the volume. This method also offers flexibility in post-processing, as planes can be selected afterward without needing to match those used during the scan. If, on the other hand, only predefined planes were of interest, measurements were limited to those specific planes. Measuring only a few planes decreased the measurement time, but limited the post-processing flexibility to only those planes.

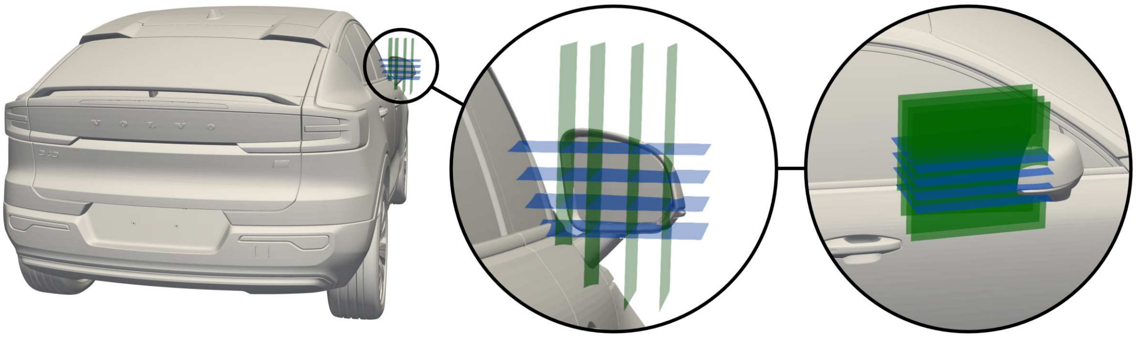

Figure 3.9: Planes creating a grid in the wake of the outer rear-view mirror.

After finishing the setup in the ProCap software, the ProCap hardware was set up in the wind tunnel. As part of this, the camera was securely mounted high up on the tunnel's slotted walls to minimize vibrations and positioned to look down at the domain at an approximately 45° angle, see Figure 3.10. The reason for this was to make it easier for the operator to angle the probe so that the reflective spheres were visible to the camera.

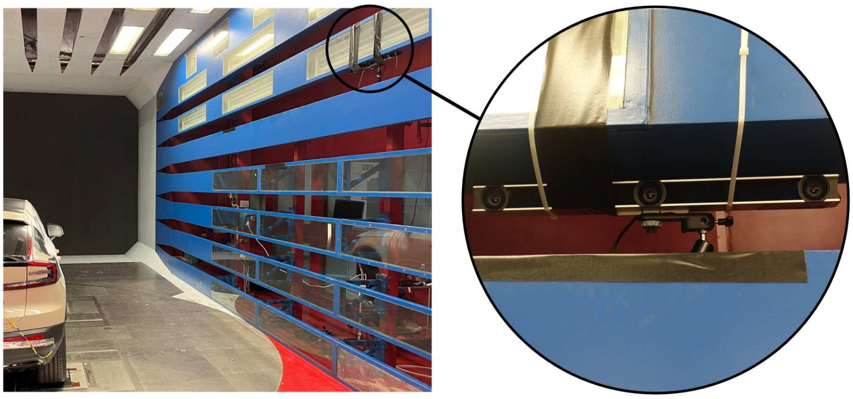

Figure 3.10: Positioning and mounting of the camera. The camera was fastened to the slotted wall with tape and stripes to reduce vibrations caused by the wind.

Finally, the camera and CAD file's coordinate systems were aligned by placing the coordinate system tool at the location of the CAD model's origin. Figure 3.11 shows the tool in use to align the coordinate systems for measuring around the mirror.

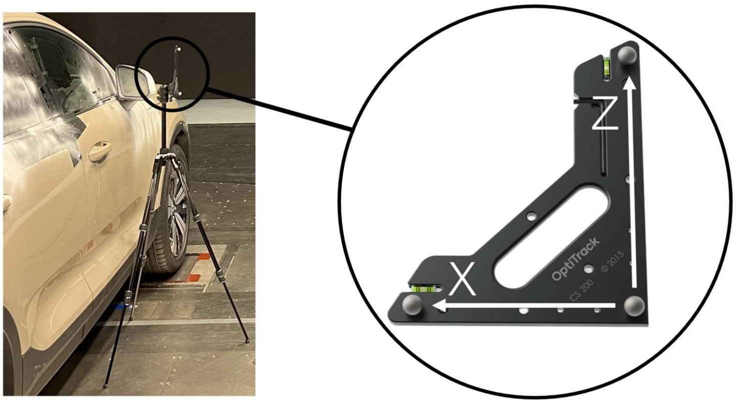

Figure 3.11: Placement of the coordinate system alignment tool for measuring around the outer rear-view mirror.

The measurements were conducted with the operator standing inside the test section or in the plenum chamber behind the slotted walls using an extension pole. When conducting measurements, the wind speed was set to 70 km/h, the operational limit for safe operator access.

During measurements, each defined plane was scanned in three steps. First, a coarse scan observing the velocity was completed to get a feeling for the general topology of the flow. Next, a convergence scan based on the 95% confidence interval was conducted to ensure data quality by minimizing and stabilizing the uncertainty. The target confidence interval was ≤ 2 m/s in stable regions and ≤ 6 m/s in unsteady areas. The reason for choosing these thresholds was that those were the lowest values that still allowed for reasonable measurement times. Choosing a lower confidence interval would have diminished the perceived advantage of the ProCap system's rapid usability. Finally, another velocity scan was completed after completing the convergence scan, focusing on removing non-physical artifacts and further increasing the data volume for the shear layers. The entire 3-step scanning procedure is illustrated in Figure 3.12. The wake can be seen to be significantly smoother and more refined after the final sweep compared to the first sweep. This is mostly due to the convergence sweep providing more measurement points in fluctuating areas of the flow. After a completed measurement, the data was exported from the ProCap software for post-processing in ParaView.

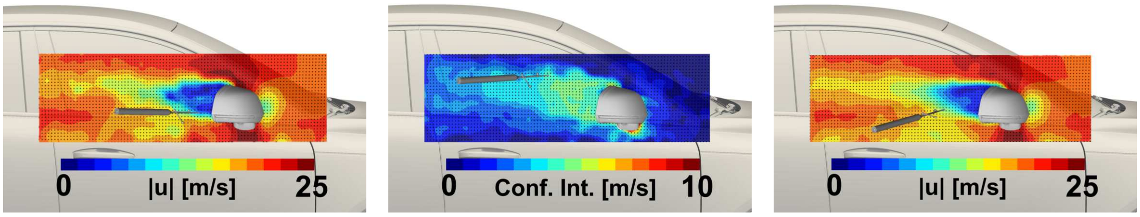

(a) Coarse velocity sweep **(b)** Convergence sweep **(c)** Final velocity sweep

Figure 3.12: Sample of the results acquired after the different sweeps.

3.3.2 Traverse-gear mounted probes

The wind tunnel is equipped with a Traverse-Gear (TG) capable of carrying a setup of two 12-hole omniprobes, shown in Figure 3.13. The main purpose of the TG is to sweep the probes in space with very high positional accuracy. The two 12-hole omniprobes are mounted on the TG with a vertical offset of 56 mm, aligned parallel to the ground plane and angled 45° to the flow. They can measure flow within a range of ±150° with an accuracy of 3% in velocity and 1.5° in flow angle [64].

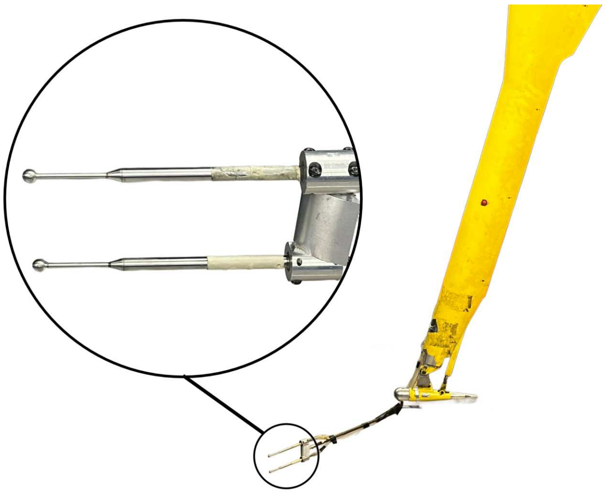

Figure 3.13: Traverse-Gear (TG) with two 12-hole omniprobes mounted.

The TG was used to scan an xz-plane. The sweep pattern implemented was to move the probes along the x-direction at constant z-levels, with a vertical step size of $\Delta z = 56$ mm and a speed of 40 mm/s. The data was sampled at 20 Hz.

The reason for using the TG in this thesis is that it has similarities to the ProCap system in terms of using pressure probes. However, compared to the ProCap it does not have any significant tracking uncertainty and has a more stable setup compared to the hand-held ProCap system. Moreover, the measurement points will be evenly distributed in each voxel when measuring with the TG, while the hand-held nature of the ProCap system can give a spatially skewed distribution of points, providing a mean velocity that is not representative of the whole voxel.

On the other hand, the TG is operated with predefined measurement points or paths, making it not possible to interactively check the results and adjust the measurement focus area, which is possible with ProCap. Also, a natural concern using the TG is its size, raising questions about its intrusiveness. However, a study by Josefsson [65] concluded that the TG only has a small effect on the flow, especially at the probe's location. Further usage of the system can also be found in [64][66]. Overall, the TG measurements are in this thesis used as a baseline due to the stable and structured measurement approach, together with the successful usage in previous works.

3.4 CFD simulation setup

The CFD simulations were run using the commercial software STAR-CCM+ version 2021.2. The unsteady IDDES method was used, with the SST k-ω URANS formulation applied close to the car's surface (turbulent near wall boundary layer region) and LES everywhere else, as described in Section 2.5.2. This work uses the same numerical setup and domain (PVT) as in Josefsson [65], which validated the setup against experimental data with good correlation.

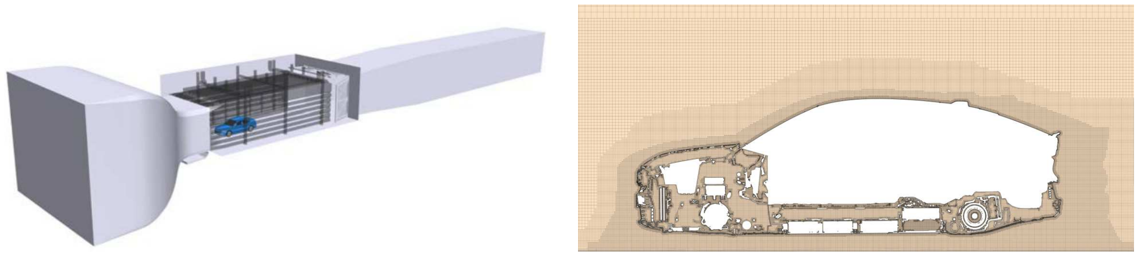

(a) Computational domain [65]

(b) Computational mesh at the $y = 0$ plane

Figure 3.14: Simulation setup used in this thesis.

3.5 System Validation and Evaluation

The ProCap system is investigated in three steps to compare and position it relative to other flow visualization techniques and simulations in terms of qualitative and quantitative performance. First, different setups and settings, as well as the system's intrusiveness, are assessed. Next, the measurements are compared with CFD simulations and the TG. Finally, the system's ability to capture changes in flow topology from different test-object configurations is evaluated. The corresponding use cases are described in detail below.

3.5.1 Base-setup evaluation

A base-setup evaluation was carried out to evaluate the robustness of the ProCap system. The evaluation is split into two parts: investigating different test setup configurations and assessing the intrusiveness of ProCap.

3.5.1.1 System and software configurations

To investigate various system settings, the outer rear-view mirror was chosen because its characteristic flow structures are representative of those observed across other regions of the vehicle. Moreover, focusing on a smaller region permits a more detailed evaluation of the voxel size sensitivity. Except for the voxel size study presented below, the same domain and plane was used for all setup evaluation measurements, shown in Figure 3.15.

The ProCap's performance is evaluated under the following conditions:

- Operator standing inside the test section, 14hp at 70 kph, measured twice for repeatability
- Operator standing inside the test section, 5hp at 70 kph
- Operator standing behind the slotted walls, 14hp at 70 kph

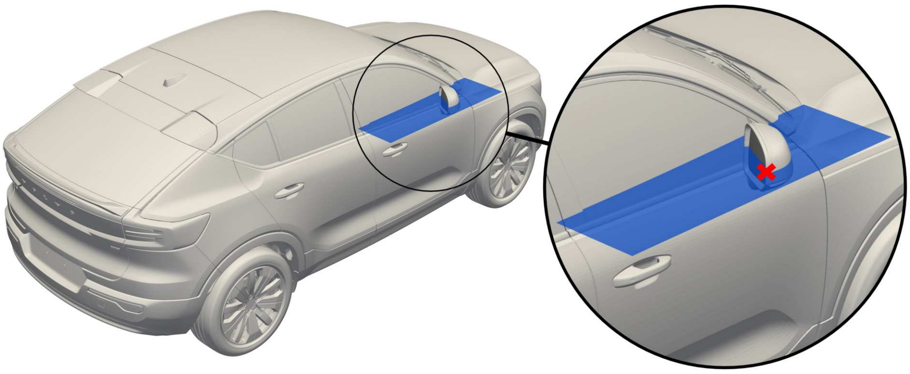

Figure 3.15: The XY-plane at $z = 1167$ mm from the ground plane, used for base-setup evaluation. The local coordinate system's origin is placed where the plane intersects the outer edge of the mirror housing, marked in red.

A voxel size study was also conducted to determine the appropriate voxel size, balancing accuracy and measurement time. The voxel sizes evaluated were 8, 13, 20, and 30 mm, using the plane shown in Figure 3.16. The reason for this measurement plane being smaller than in Figure 3.15 was to save measurement time, as it was assumed that changes induced by varying the voxel size would be most prevalent close behind the mirror.

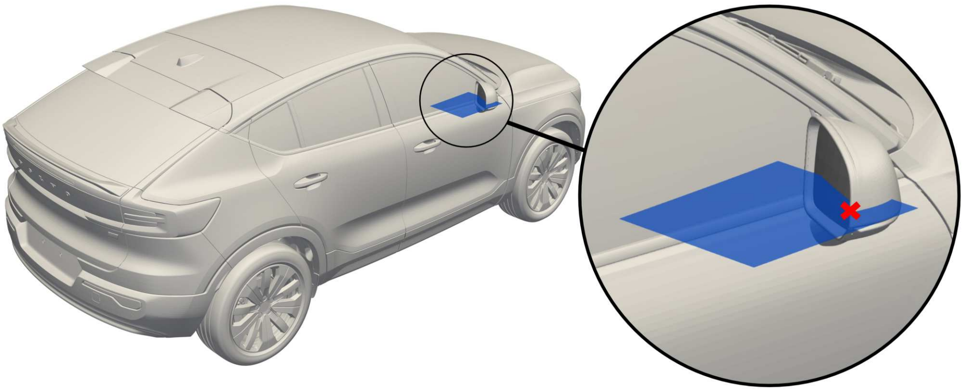

Figure 3.16: The XY-plane at z = 1133 mm from the ground plane, used for the voxel size study. The local coordinate system's origin is placed where the plane intersects the outer edge of the mirror housing, marked in red.

3.5.1.2 Intrusiveness study

The intrusiveness of the ProCap test setup, including the operator, was also evaluated. To do so, a CFD simulation was conducted where a modeled operator was introduced to evaluate potential changes to local flow structures in the vicinity of the measurement region. The geometry of the operator is shown in Figure 3.17. To isolate the influence of the operator, an additional simulation was performed with the probe in the same position but without the operator geometry.

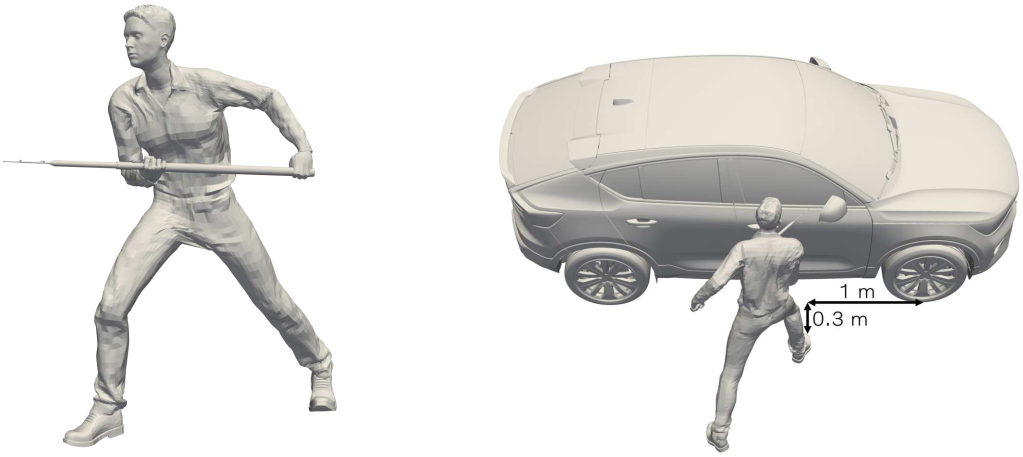

(a) The modeled operator **(b)** The operators position relative to the test object

Figure 3.17: The modeled operator used for simulation.

3.5.2 Comparison between ProCap measurements, CFD simulations, and TG measurements

To assess the validity of the ProCap measurements, ProCap scans were compared to results from CFD simulations and the traverse-gear system. The following regions of the car were investigated:

- Base wake
- Outer rear-view mirror
- Antenna

The regions were selected because they exhibit diverse wake sizes: the base generates the largest wake, the outer rear-view mirror an average one, and the antenna the smallest. Figure 3.18 illustrates the measurement plane used for each area. For the base wake, a comparably large voxel size of 33 mm was used to prevent excessively long measurement times. Conversely, the antenna was measured with a small voxel size of 4 mm to test the ProCap's ability to provide high-resolution data where small flow structures are present. Finally, the outer rear-view mirrors used a 13 mm voxel size, as this was shown to be the best compromise for that area in Section 4.1.1.

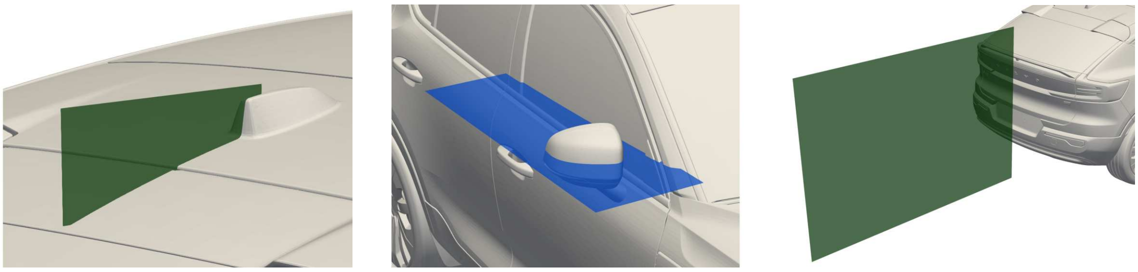

(a) Antenna, XZ plane at $y = 0$ mm (centerline)

(b) Outer rear-view mirror, XY plane at $z = 1167$ mm from the ground plane

(c) Base wake, XZ plane at $y = 0$ mm (centerline)

Figure 3.18: Planes used for comparison with CFD simulations and the traverse-gear probe.

All measurements with the ProCap system for this section were done with the 14hp, standing inside the test section at 70 kph. The plane for the base wake was also scanned with the TG. The outer rear-view mirror and antenna were not measured using the TG due to safety concerns, as the setup would require the gear to operate in close proximity to the vehicle surface.

3.5.3 Geometry modification investigation

This study is aimed at evaluating the ProCap system's ability to capture changes in flow structure resulting from local geometric modifications to the car. The first modification was to remove the rear wing, and the second was to add a 20 mm z-kick to the rear edge of the roof, illustrated in Figure 3.19. The measurement plane for the roof-kick is shown in Figure 3.20. The voxel size used for the kick measurement was 13 mm because it has similarly sized flow structures as the outer rear-view mirror, and this voxel size will later be shown to be the best compromise for such areas. For the rear wing (base wake), the same voxel size and measurement plane is used as in Section 3.5.2.

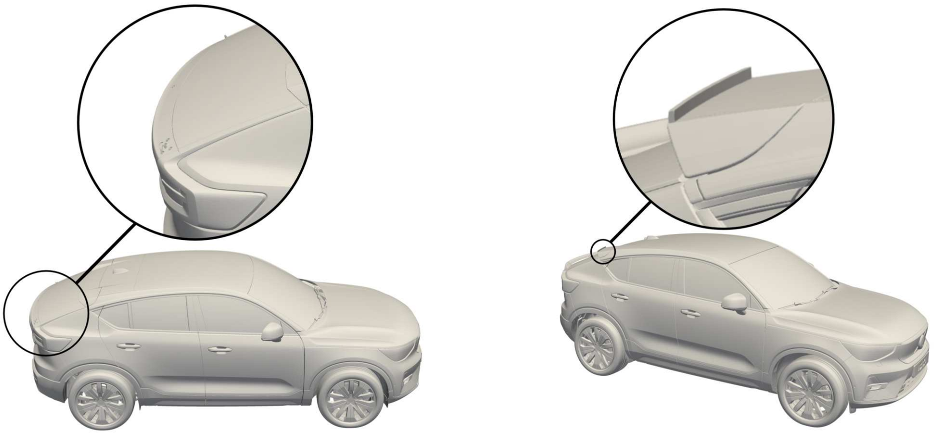

(a) Rear wing removed. **(b)** Roof-kick added.

Figure 3.19: The two modified cars for the configuration deltas.

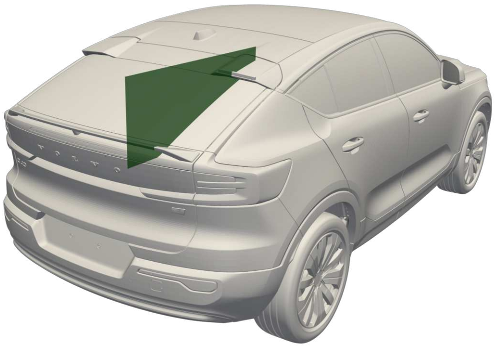

Figure 3.20: Measurement plane used for investigating the addition of a roof-kick.

4

Results

In this chapter, the results from the three evaluation steps - base-setup evaluation, comparison between ProCap measurements, CFD simulations, and TG measurements, and geometry modification investigation - are presented and discussed. The results are analyzed from both a qualitative and quantitative point of view.

4.1 Base-setup evaluation

The ProCap system can be configured in multiple ways. Therefore, an investigation was conducted to determine which setup is most suitable for this thesis, as well as giving general recommendations on how to use the same in the Volvo Cars aerodynamic wind tunnel. Additionally, the intrusiveness of the ProCap system, including the operator, was investigated in terms of CFD simulations.

4.1.1 Voxel size study

The voxel size is considered the most important software setting, which is why a sensitivity study was conducted around the outer rear-view mirror. The resulting velocity fields are shown in Figure 4.1, showing that the larger the voxel size, the smoother the velocity contour. This trend resembles finite volume discretization, where the usage of coarser mesh sizes filters the smaller flow structures and related fluctuations. The observed smoothing with increased voxel size can be attributed to the averaging of measurement points within each voxel. A larger voxel typically contains more points, making it less affected by fluctuations.

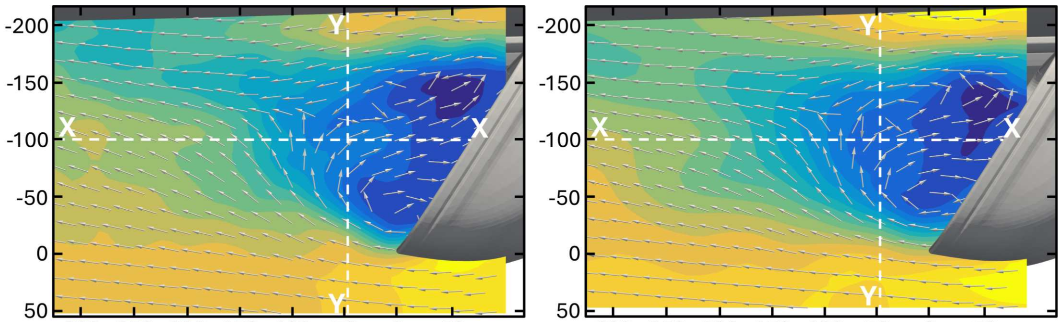

(a) 8 mm **(b)** 13 mm

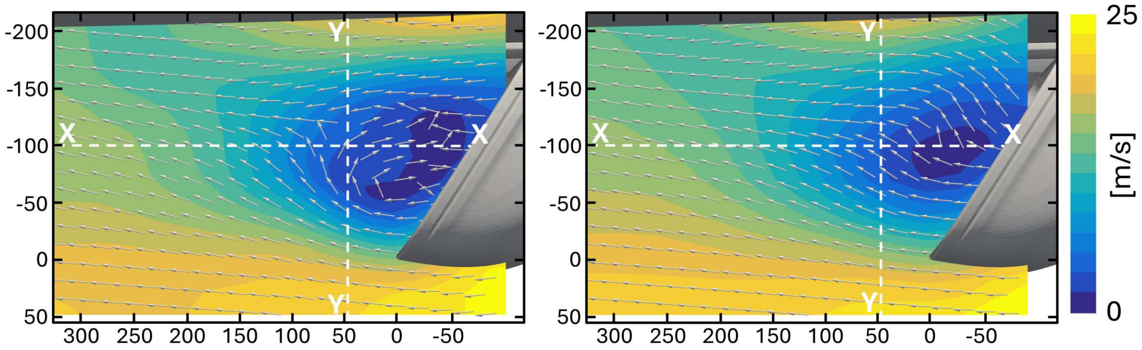

(c) 20 mm **(d)** 30 mm

Figure 4.1: Z-planes showing velocity magnitude from the voxel study.

Inherently, the ProCap system can identify the locations of large-scale vortical structures within the measurement region. The vortical structures in the mirror wake can be seen to be captured similarly for the 8 and 13 mm voxel sizes. The 20 mm scan also captures the vortex structure reasonably well, but the 30 mm mesh does not indicate any such structures. This is a clear indication that large voxels filter out flow structures with relatively small length scales.

For a quantitative comparison between the voxel sizes, the u_x velocity component was used since u_y and u_z components were comparatively lower and added additional noise to the measurement data. This is likely due to the low, unsteady velocities measured for these components, which lie outside of the probe's calibration region.

The velocities along the X-X line in Figure 4.2a show a converging trend where the velocities get closer to the finest mesh size as the voxel size decreases. It can also be noted that as the distance to the mirror grows, the difference between the voxel sizes decreases. The reason for this is that the velocity gradients are smaller, and the unsteadiness of the flow decreases the more the wake disperses, making the averaging effect of the larger voxels not as evident. At first glance, u_x for the Y-Y line at around $y = -180$ mm, shown in Figure 4.2b, looks to contradict this, but it follows the mentioned trend because the boundary layer from the side of the car creates significant velocity gradients, preventing convergence.

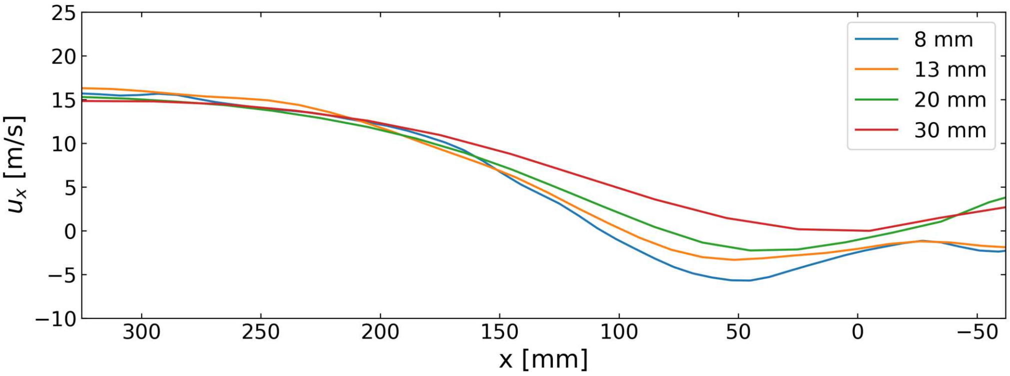

(a) Velocity along the X-X line

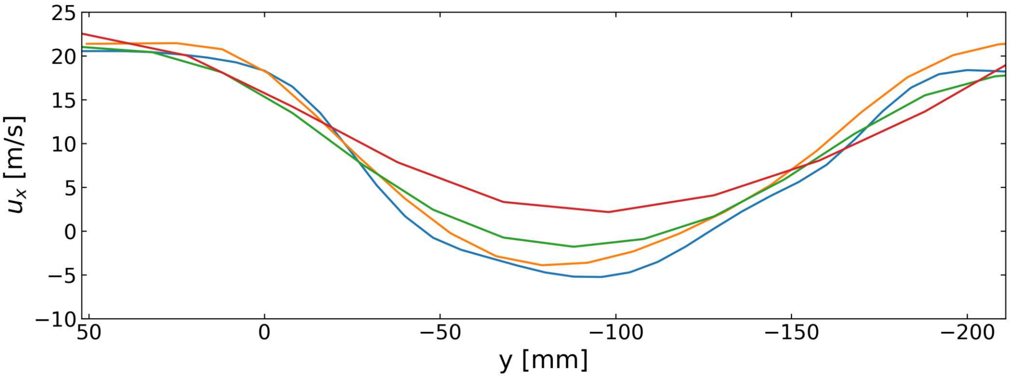

(b) Velocity along the Y-Y

Figure 4.2: The u_x velocity component on the lines from Figure 4.1.

Another trend shown in Figure 4.2b, between $y = -50$ to 0 mm, is that the velocity gradient gets larger with smaller voxel sizes. This means that the shear layer gets thinner with decreasing voxel size, explained by the larger voxels' wider averaging distances. However, the same trend is not present at $y = -200$ to -130 mm for the 8, 13, and 20 mm voxel sizes, which can be attributed to the gradient not being steep enough to emphasize the averaging effect of the larger voxel sizes.

The topology of the separation bubbles is shown in Figure 4.3. The coarsest mesh, 30 mm, captures the topology reasonably well on the far side from the car but misses substantially on the side of the mirror closest to the car, compared to the finest mesh. While it is not physically feasible for the wake to start outside of the mirror, it does so for the largest voxel size because the same voxel can partly be located behind the mirror and at the same time in the free-stream. Conversely, for the 20 mm voxel size, the wake topology is closely captured for most parts. The only difference from the finest mesh is that the 20 mm scan does not have a clearly defined tip at the downstream-most part of the wake. Looking at the 13 mm mesh, it has a tip at the end of the bubble, but it is not as sharp as for the 8 mm mesh. Overall, the wake topology shows a converging trend towards the 8 mm (finest) voxel size.

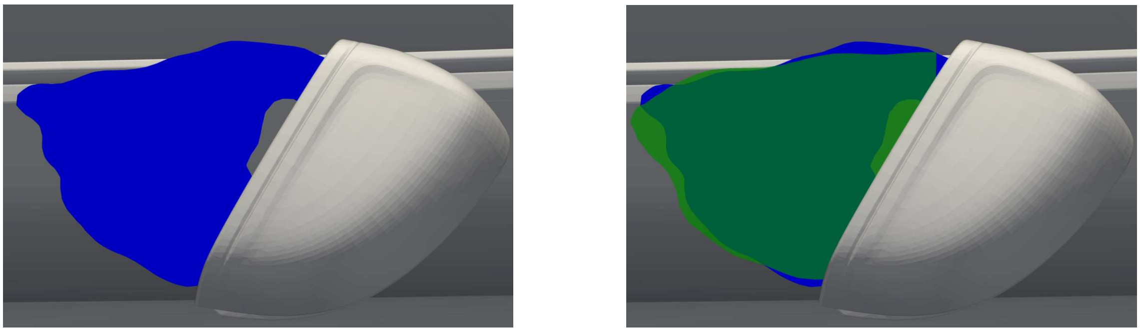

(a) 8 mm

(b) 13 mm (green) compared to 8 mm (blue)

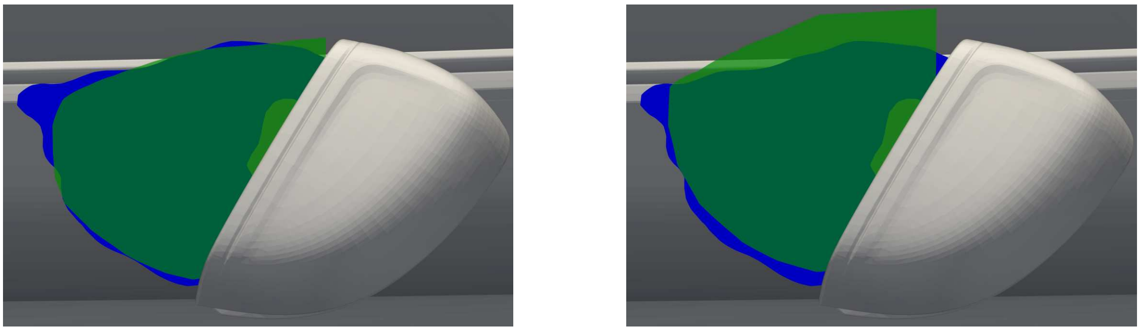

(c) 20 mm (green) compared to 8 mm (blue)

(d) 30 mm (green) compared to 8 mm (blue)

Figure 4.3: Isosurfaces of $c_{p,tot} = 0$ for the different voxel sizes projected on the same plane as Figure 4.1.

Reducing mesh size had little impact on measurement time for the 30, 20, and 13 mm meshes; however, the 8 mm mesh more than doubled the measuring time compared to the larger sizes. The measurement times are presented in Table 4.1.

Table 4.1: Measurement time for the respective voxel sizes.

Voxel size [mm]	Meas. time [min]
8	41
13	19
20	18
30	16

From Table 4.1, it is evident that the 13 mm voxel size proved to be the best compromise between accuracy and measurement time. This was because the 13 mm mesh gave a reasonable numerical convergence with the 8 mm mesh, a sufficient accuracy in capturing the separation bubble, and its efficiency regarding measurement duration. Further measurements around the mirror were therefore concluded with a 13 mm voxel size, and this size is recommended for similar measurement scenarios. However, if a very high accuracy of flow structures is desired, and measurement time is not a constraint, 8 mm or even smaller voxel sizes are recommended. If, instead, measurement time has the highest priority, a larger voxel size can be used, but it should not exceed 20 mm, as this significantly compromises the measurement quality.

4.1.2 Measurement repeatability

To evaluate the repeatability of measuring with the 14hp while having the operator standing in the test section, the same measurement was repeated twice. The resulting velocity plot is shown in Figure 4.4.

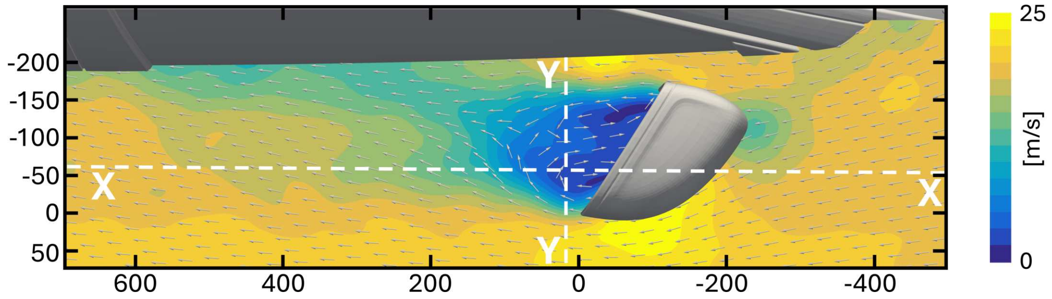

(a) The velocity contour from the first (baseline) measurement.

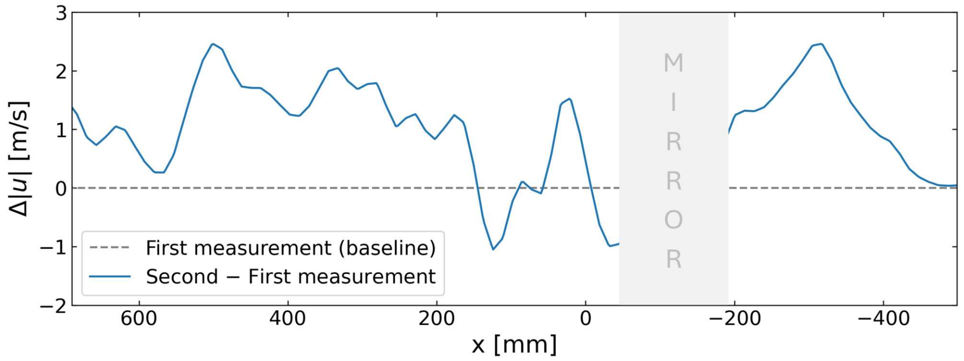

(b) The $|u|$ delta between the first and second measurement on the X-X line

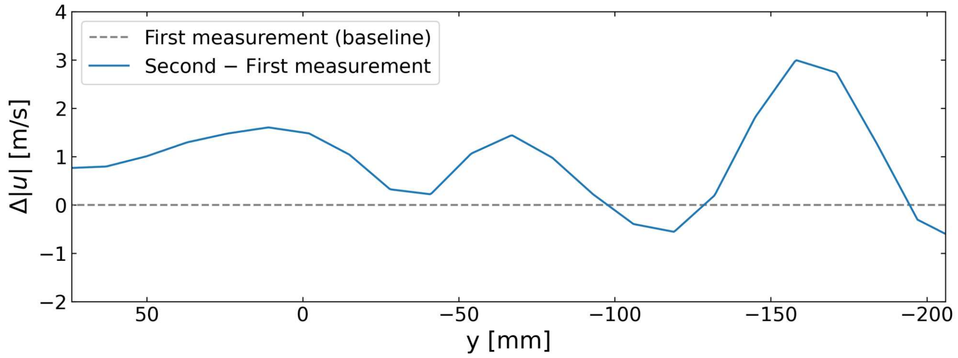

(c) The $|u|$ delta between the repeated measurements on the Y-Y line

Figure 4.4: Velocity contour and delta plots for the repeat of the same measurement.

The delta plots in Figures 4.4b-c have a 2σ standard deviation of 1.9 m/s (10.0% of free-stream velocity) and 1.7 m/s (8.7%) for the X-X and Y-Y lines, respectively. This is significantly higher than the 2σ standard deviation from the probe calibration, which was 0.41 m/s (1.2% of calibration velocity). The following sources of error, which also apply to subsequent measurements in this thesis, were identified as contributing to the higher standard deviation:

- The calibration procedure is conducted in steady flow conditions. That is not true for the flow around the mirror, where pressure fluctuations on the probe tip may not be in sync over the whole tip.
- The flow's unsteady nature makes it possible to measure different values at the same position, requiring more measurement points added to each voxel to average out the fluctuations.
- The flow velocity is outside of the probe's calibration range (20-64 m/s).
- Inaccuracies in the position-tracking of the probe, placing measurement points in the wrong voxels.
- Variation in the operator's position and body orientation, varying the extent of intrusive effects.

To reduce these error sources, the scanning method using the confidence interval was used. Considering the 95% confidence interval ($\approx 2\sigma$ standard deviations) threshold was set to 6 m/s for unsteady regions and 2 m/s for steady flow regions, the standard deviations obtained from the repeatability study are acceptable (lower) and can therefore be considered repeatable. Of course, choosing lower thresholds would decrease the error further, but would also extend measurement time, diminishing the system's advantage of being fast to use.

4.1.3 Pressure probe choice - 5hp vs. 14hp

Comparing the results from the 14hp and 5hp the main differences are found in the separation bubble right behind the mirror. The 5hp measurement does not show any recirculation, while the 14hp does, as can be seen in Figure 4.5. This is because the 5hp has a ±60° angle of acceptance and was pointed in the upstream direction of the tunnel, which resulted in the negative x-direction not being captured by the probe. With the much larger angle of acceptance of the 14hp, capturing the recirculation was not an issue. Despite this, the 5hp still captures the wake topology similar to the 14hp shown in Figure 4.4a. Also note that it was not possible to reach between the mirror and the side window with the tip of the 5hp while the reflective spheres were visible to the camera, creating a gap in the data.

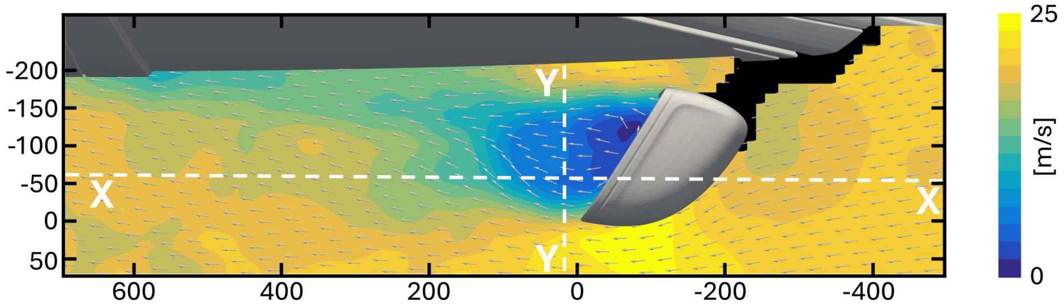

Figure 4.5: Velocity contours from the 5hp.

Figure 4.6 compares the u_x components from the 14 and 5hp. It shows a high delta behind the mirror where the u_x directions are opposite between the probes because the 5hp does not capture backflow. Despite the initially high deltas behind the mirror, further away from the mirror, the difference between the probes is low, mostly below 1 m/s. This shows that although the 14hp has a calibration range of 20-64 m/s, it still has good accuracy at lower velocities. The lowest velocity where the probes match is at around $x = 130$ mm, where the velocity is 7 m/s.

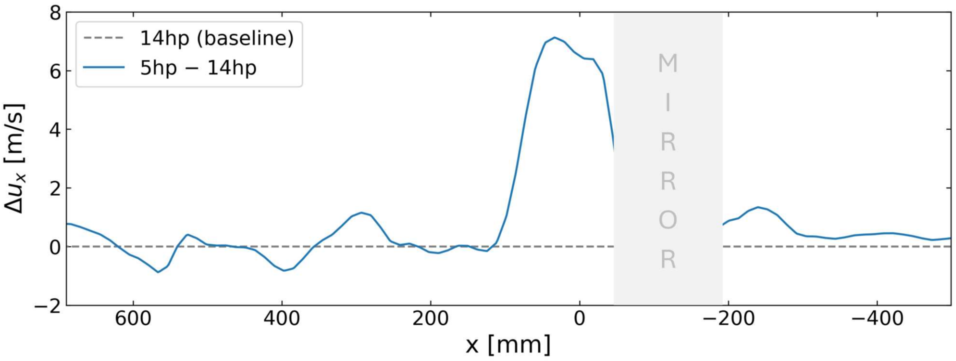

Figure 4.6: The u_x delta along the X-X line between the 14hp and 5hp.

With the ability to capture reverse flow, being able to collect data in the whole domain, and at the same time showing good accuracy even at lower velocities, the 14hp was considered to be more suitable than the 5hp for scanning the outer rear-view mirror and areas with similar flow topology. The 14hp is therefore used for the remainder of the thesis.

4.1.4 Measuring from the test section vs. behind the slotted wall

The total velocity delta between standing in the test section during a measurement compared to standing behind the slotted walls is shown in Figure 4.7. It shows that the difference between these two methods falls within the repeatability error for the X-X line, with a 2σ standard deviation of 1.5 m/s compared to 1.9 m/s from the repeatability scans. For the Y-Y line, the same is not true, having a 2σ standard deviation that is 0.5 m/s larger than the repeatability. This indicates that intrusive effects could be affecting the wake in the y-direction.

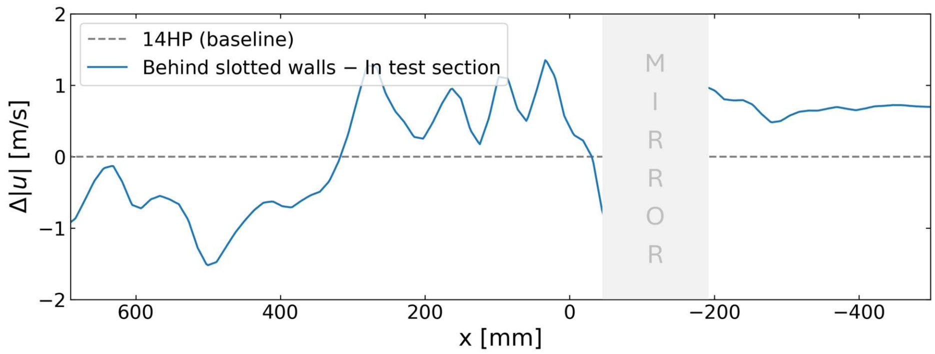

(a) X-X line

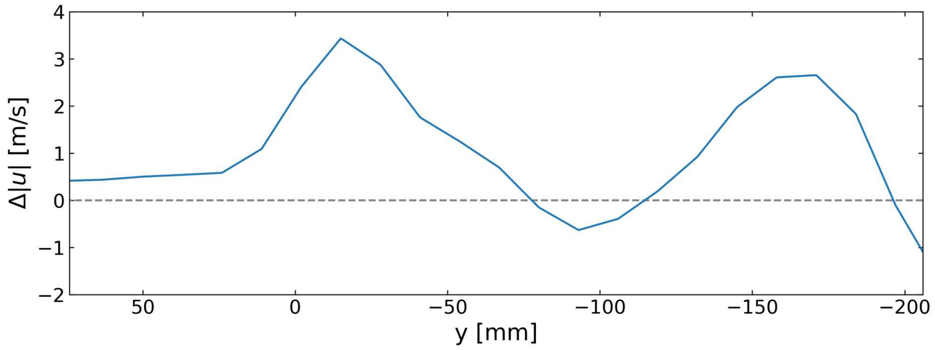

(b) Y-Y line

Figure 4.7: Velocity deltas between measuring from the plenum and in the test section.

To further investigate the intrusiveness of having an operator standing close to the car, CFD was used to simulate such a scenario. The resulting separation bubble topologies from the different scenarios are illustrated in Figure 4.8. It can be seen that the operator shields the car, deflecting the mirror's wake towards the car, and slightly shortening it. Conversely, only having the probe, without the operator, gives almost no difference in wake topology. It shows that the main intrusive feature is the operator and not the probe itself.

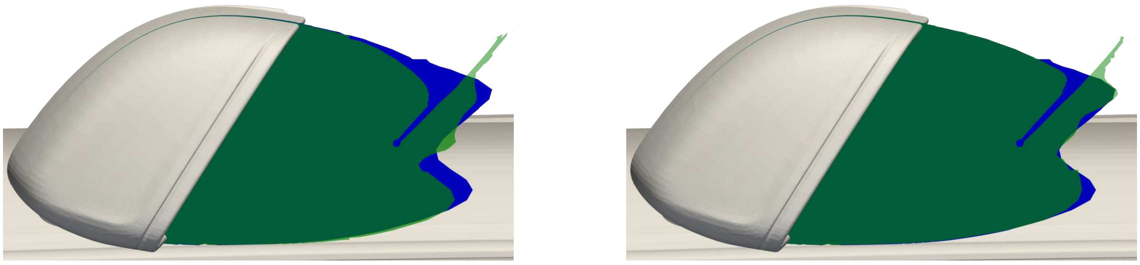

(a) Operator and probe **(b)** Only probe

Figure 4.8: Isosurfaces $c_{p,tot} = 0$ from CFD simulations showing the wake topology when adding intrusive components (green) against only having the car (blue).

While conducting the ProCap measurements, it proved to be more difficult to operate and sweep the probe accurately from behind the slotted walls compared to standing in the test section, extending the measurement time by a factor of 2.5. The significant increase in measurement time was considered too large to justify the reduced intrusiveness, so the decision was made to conduct the remaining measurements standing in the test section.

Building on this conclusion, together with the findings in Section 4.1.3, measuring from the test section with the 14hp was selected as the measurement configuration for the remainder of the thesis.

4.2 Comparison between ProCap measurements, CFD simulations, and TG measurements

ProCap measurements taken at different regions around the test vehicle are presented in this section, alongside a comparison with CFD simulations and TG measurements.

4.2.1 Base wake

In addition to ProCap and CFD results, the base wake was measured using the traverse-gear system (TG). The TG system is used as a baseline due to its stable setup, structured measurement approach, and its successful use in other works, as discussed in Section 3.3.2. Figure 4.9 shows the velocity contours from the three methods.

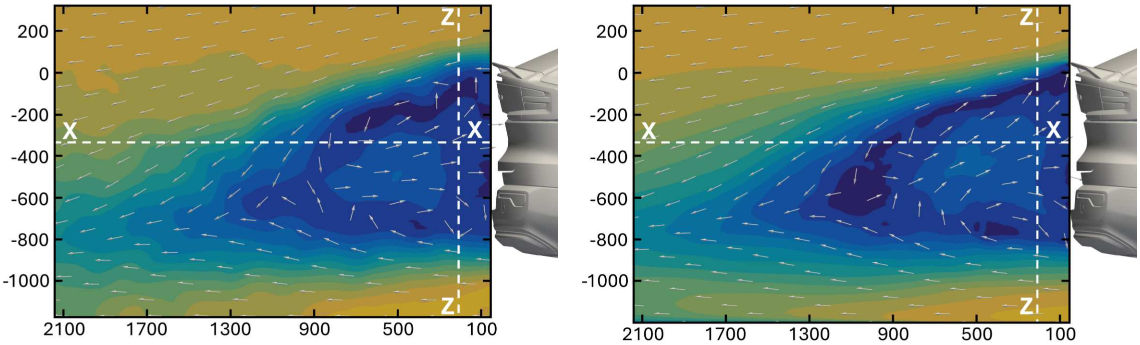

(a) ProCap **(b)** CFD

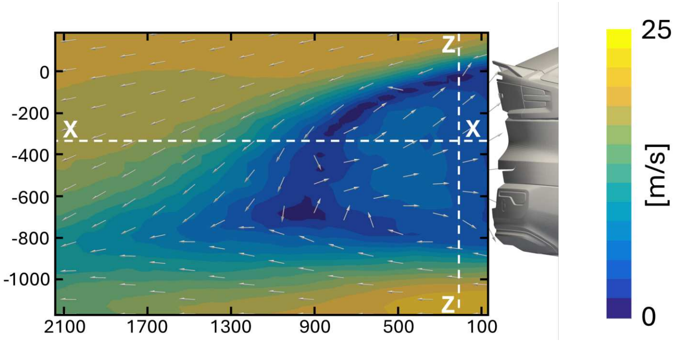

(c) TG

Figure 4.9: The velocity contours from measuring and simulating the base wake.

One difference between ProCap and the other two methods is that ProCap gives a thicker shear layer than both CFD and TG. The reason for this is attributed to the large voxel size and interpolation scheme, as well as the limited accessibility close to the wing. This is further emphasized in Figure 4.10, where the differences in velocity gradients above the separation bubble are seen at $z = 0$ to 180 mm. As discussed in Section 4.1.1, a smaller voxel size, when combined with ProCap's interpolation scheme, would produce a steeper gradient. Interestingly, the ProCap system does not have issues capturing the shear layer velocity gradient from the diffuser at $z = -1100$ to -800 mm. This showcases that the voxel size and interpolation scheme do not play as large of a role for more shallow gradients.

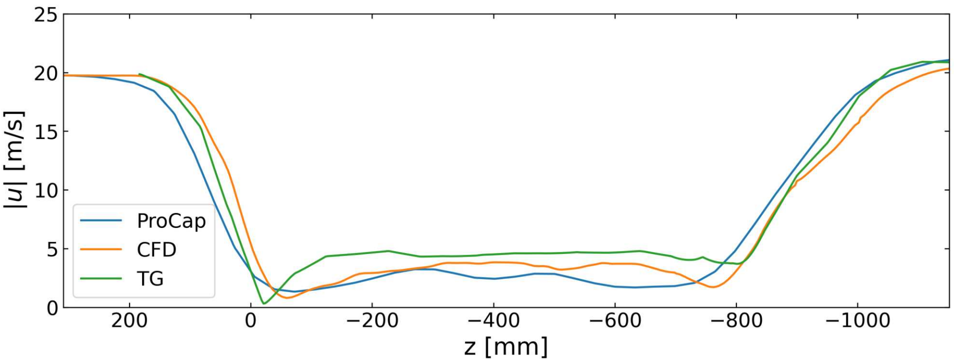

Figure 4.10: Velocity magnitude for ProCap, TG, and CFD at the base wake along the Z-Z line defined in Figure 4.9.

Another aspect noticed in the contour plots above, Figure 4.9, is the additional unsteadiness in the ProCap measurements. The transition across the shear layers in the wake is markedly wavy, indicating another deficiency of this technique. The reduced waviness observed in the TG shear layers can be attributed to the more stable probe motion. Conversely, the ProCap system shows a tendency to be wavy due to operator-induced factors (uneven measurement point distribution within voxels, speed of probe motion, etc.). The reason for the lack of waves in the CFD simulations is that it smooths out fluctuations smaller than the chosen finite volume mesh size, leading to a more continuous shear layer transition.

Figure 4.11, showing the results along the X-X line, confirms the trend regarding ProCap's accuracy for shallow gradients. Here, the ProCap measurement has a 2σ standard deviation of 1.9 m/s (9.8%) to the TG, compared to 2.6 m/s (13.4%) between the CFD and TG. This shows that the ProCap system is more accurate than CFD for areas with shallow gradients, while CFD gives a more accurate prediction for sharp gradients.

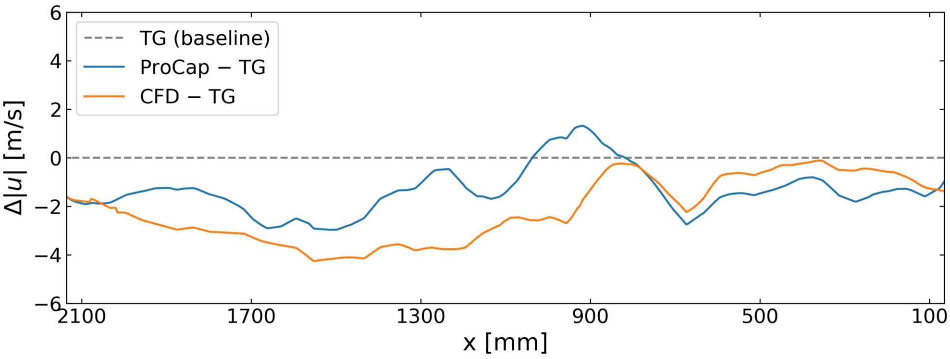

Figure 4.11: Velocity deltas compared to TG for ProCap and CFD at the base wake along the X-X line defined in Figure 4.9.

Looking at the separation bubbles, shown in Figure 4.12, ProCap and CFD also seem to have different strengths. Despite ProCap overestimating the thickness of the shear layer close to the rear wing, it captures the separation bubble better than

CFD does close to it. Conversely, the CFD simulation shows good agreement on the downstream part of the bubble, where the ProCap's wake is too narrow. The reason for ProCap's narrowing at the tip of the bubble, which looks like a dent, could be due to measuring points in the present voxel being over-represented with points close to the free-stream. This would give the voxel a higher velocity and a higher total pressure coefficient, not including it in the figure. On a side note, all three methods show reasonable agreement on the lower half of the isosurface.

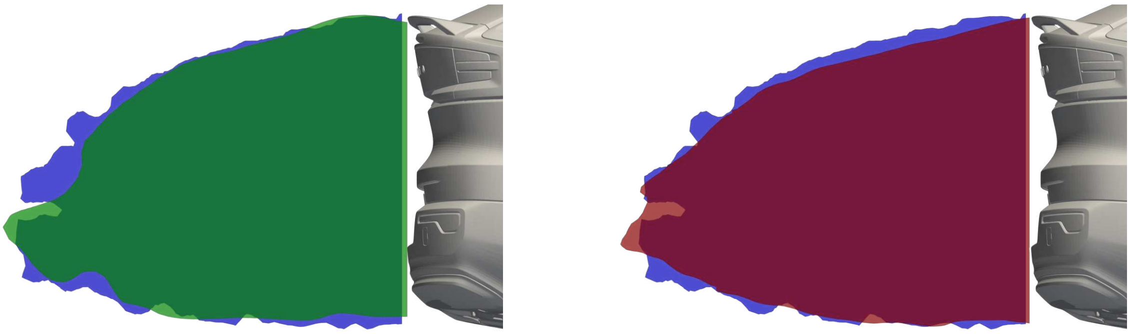
(a) ProCap (green) and TG (blue)

(b) CFD (red) and TG (blue)

Figure 4.12: Wake topology for ProCap and CFD compared to TG with isosurface $c_{p,tot} = 0$ projected on the $y = 0$ plane.

Overall, while not being identical, the overall size and shape of the separation bubbles observed with ProCap, CFD, and TG are reasonably consistent. This consistency reflects both the capability of the ProCap system and the reliability of the CFD method used.

4.2.2 Outer rear-view mirror

Several differences can be observed when comparing velocity contours from ProCap and CFD around the outer rear-view mirror, as shown in Figure 4.13. One notable difference is that the CFD simulations predict lower velocities at the stagnation point directly behind the mirror, which could be due to the voxel averaging effect. Another notable difference is observed in the flow acceleration between the mirror and the side window. While CFD captures this phenomenon, ProCap measurements consistently underestimate the velocities within this region. This is because the interpolation scheme employed by ProCap carries the lower velocity from behind the mirror and shear layer to the high velocity area. This effect would likely be mitigated with a smaller voxel size, preventing the lower velocity from being carried all the way to the high velocity zone. Furthermore, the vortex behind the mirror on the far side of the car is located closer to the edge of the mirror for CFD compared to ProCap. The reason for this could be a combination of the presence of the operator pushing the vortex inward, together with the shear layer's increased thickness for the ProCap measurement.

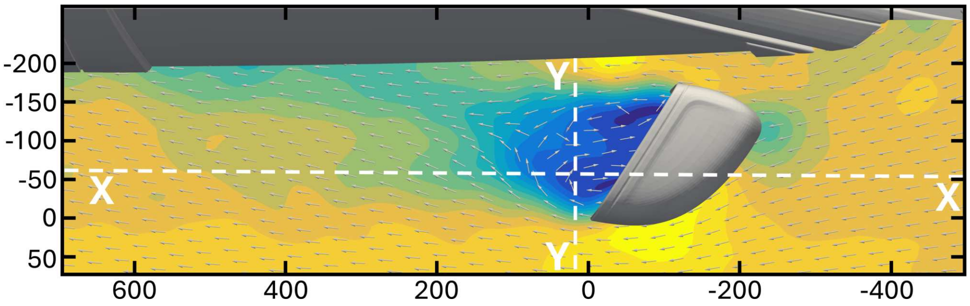

(a) ProCap

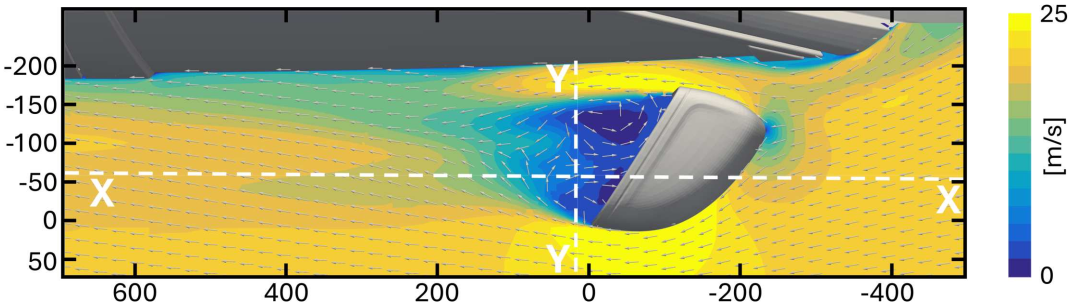

(b) CFD

Figure 4.13: Velocity contours for ProCap and CFD around the outer rear-view mirror.

Despite these differences, several similarities exist when observing the plots from a macro-perspective:

- The flow is accelerated around both sides of the mirror (but to varying degrees).
- The wake is angled towards the car.
- The far wake hits the side window approximately at half of the window's width.
- Similar mirror wake topology with two distinct recirculation zones close to the mirror.

According to Figure 4.14a, the quantitative difference between the two methods is the largest in the separation bubble. The further downstream from the mirror, the more similar the velocities are. A familiar trend from the base wake results is also apparent in Figure 4.14b: the shear-layer is significantly thicker for the ProCap measurements compared to CFD, characterized by the difference in velocity gradients. Additionally, ProCap is not able to capture the boundary layer close to the car, which CFD does. Even with a very small voxel size, this would be challenging due to the physical dimensions of the probe tip preventing it from reaching to the surface, as well as creating disturbances for the measured flow. The ProCap system is therefore not suited for measuring flow close to surfaces.

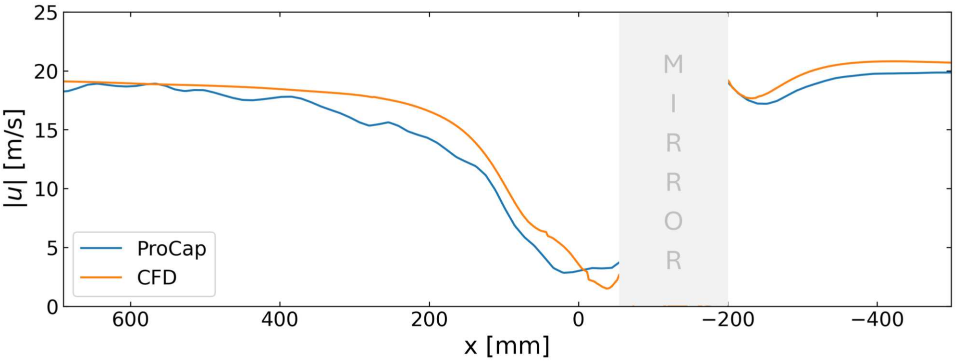

(a) Velocity magnitude for ProCap and CFD on the X-X line

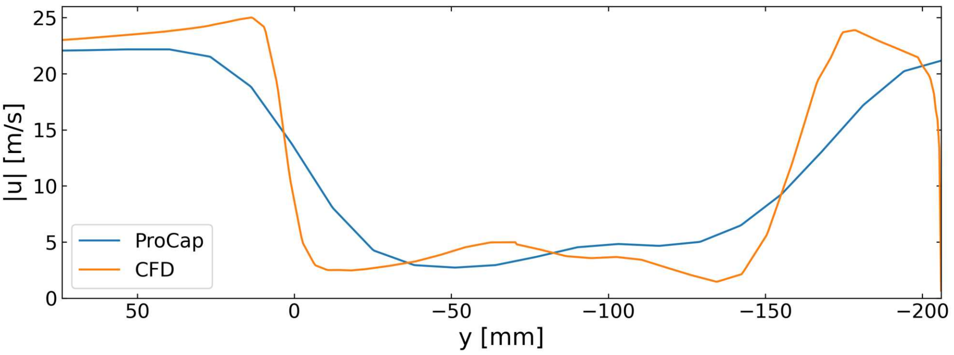

(b) Velocity magnitude for ProCap and CFD on the Y-Y line

Figure 4.14: Numerical comparison between CFD and ProCap around the side-view mirror.

Despite differences in velocity contours between ProCap and CFD, their separation bubble topologies exhibit strong similarities, as illustrated in Figure 4.15. A key distinction is the presence of a far-field wake bifurcation in the CFD separation bubble, which is also evident in its velocity contour but absent in the ProCap results. Furthermore, the inwash from the surface of the mirror furthest away from the car is more pronounced in the ProCap measurements, which could be due to the additional blockage from the operator (as described in section 4.1.4). Overall, the separation bubble topologies from CFD and ProCap can be considered similar, particularly when the approximate wake topology is the primary focus.

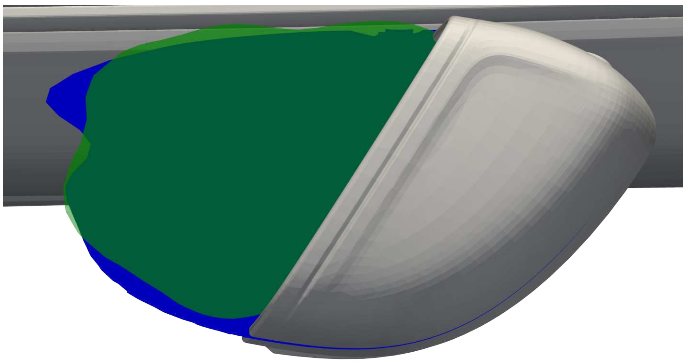

Figure 4.15: Isosurface $c_{p,tot} = 0$ for CFD (blue) and ProCap (green) projected on the plane from Figure 4.13.

To compare the vortical flow structures captured by CFD and ProCap, an isosurface of the Q-criterion is shown in Figure 4.16. While there are larger differences immediately behind the mirror, the interesting feature is the long vortex traveling downstream. CFD and ProCap portray this structure very similarly, with the location being almost identical, and ProCap indicating only a slightly longer structure compared to CFD. That the ProCap system is able to capture rotational structures accurately confirms the findings from Bartl et. al. [61]. Being able to visualize vortices accurately is of great importance because they have a large effect on the overall aerodynamic performance of a car, as discussed in Section 2.1.2.

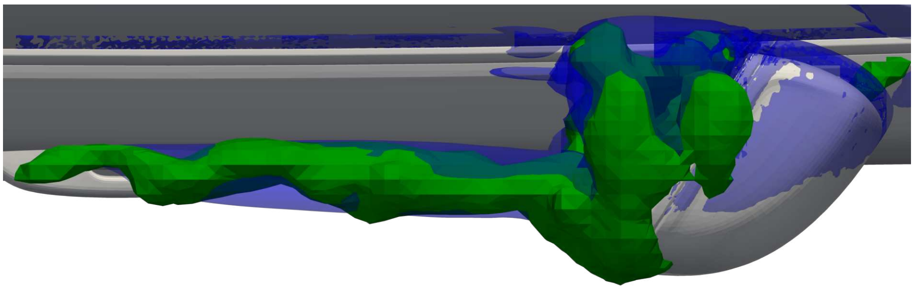

(a) Top-view

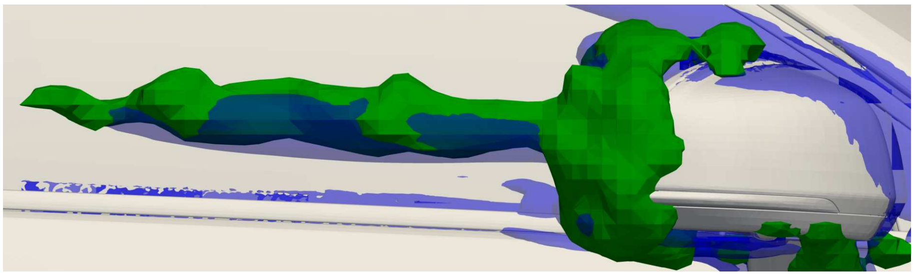

(b) Side-view

Figure 4.16: Isosurface of Q-criterion = 10 000 s^{-2} from CFD (blue) and ProCap (green).

As for the base wake in the previous section, ProCap and CFD show differences when taking a deeper look into velocity contours and their numerical values, but exhibit strong agreement regarding overall flow topology, including rotational structures.

4.2.3 Antenna

The antenna is the area investigated where the largest differences between ProCap and CFD are spotted, as shown in Figure 4.17. One significant difference is that the downwash from the edge of the antenna is more pronounced in CFD when compared to ProCap. Furthermore, despite the short low-velocity zone behind the antenna and rapid flow reattachment, a thick boundary layer still appears to travel downstream. This type of boundary layer can not be seen in the CFD. It is reasonable for the flow this far back on the car to have a significant boundary layer build up, but there is a risk that ProCap overestimates it, just as for the shear layer per previous sections. On the other hand, the voxel size study in Section 4.1.1 showed that the overestimation of the boundary layer reduces with voxel size, and the 4 mm voxel size used for the antenna can be considered very small. However, having such a small voxel size, smaller than the size of the probe tip, could potentially also be problematic by itself and present an error source.

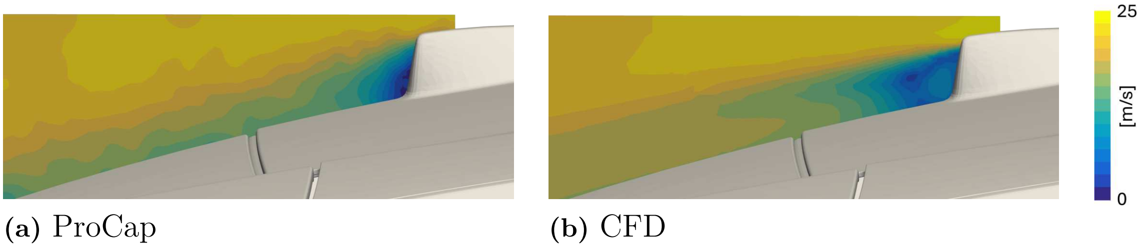

(a) ProCap (b) CFD

Figure 4.17: Velocity contours for ProCap and CFD at the antenna.

As evidenced by the velocity contour, the separation bubble is significantly smaller for ProCap compared to CFD, shown in Figure 4.18. This difference is large enough to influence the local aerodynamic behavior of such features.

Figure 4.18: Isosurface $c_{p,tot} = 0$ for ProCap (green) and CFD (blue) at the antenna projected on the plane from Figure 4.17.

The large differences between the ProCap measurement and the CFD simulation make the antenna an interesting area for further investigation, as a representation of measuring small flow features. What speaks for the ProCap is that it has shown good alignment for the previous areas regarding flow topology. On the other hand, the small voxel size and the physical size of the probe head likely act as a significant error source. Additionally, measuring such a small domain, the significance of inaccuracies from the camera system increases. In conclusion, ProCap measurements around small features can possibly generate unphysical results when the voxel size is smaller than the probe diameter and should be interpreted cautiously.

4.3 Geometry modification investigation

Having established the ProCap system's accuracy against CFD and the traverse-gear system, its typical use case - visualizing changes in flow topology when applying geometrical vehicle modifications - is investigated. To do so, two different configurations are compared with the baseline. The first configuration has an added kick to the roof spoiler, changing the flow over the rear window, and the second configuration has a removed rear wing to change the topology of the base wake.

4.3.1 Adding a roof-kick

The ProCap measurements show that the velocity field changes significantly when a 20 mm kick is added to the roof's separation edge, as shown in Figure 4.19. The kick can be seen to direct the flow further upward in comparison with the baseline. Moreover, the separation area after adding the kick is therefore significantly larger, and the flow velocity in the wake is lower at the rear wing.

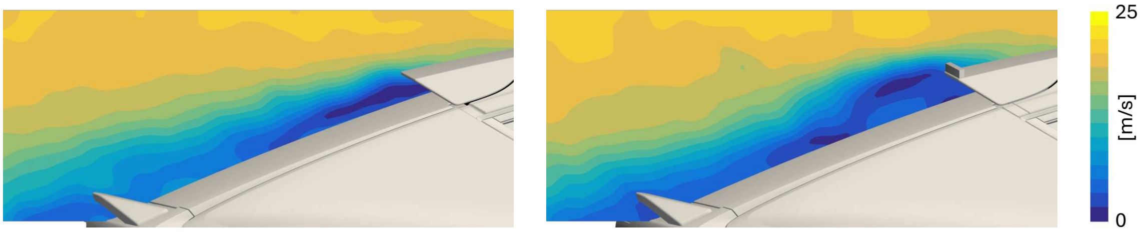

(a) Baseline **(b)** Roof-kick

Figure 4.19: Velocity contours for the geometrical changes to the roof's separation edge.

Having a closer look at the separation bubbles, illustrated in Figure 4.20, it is shown that adding the kick not only lifts the bubble higher up but also widens it. Consequently, a desirable property of the baseline's wake — its impingement on only the outermost part of the wing — is diminished with the addition of the kick. This likely results in reduced rear wing downforce due to the decreased momentum of the impinging airflow.

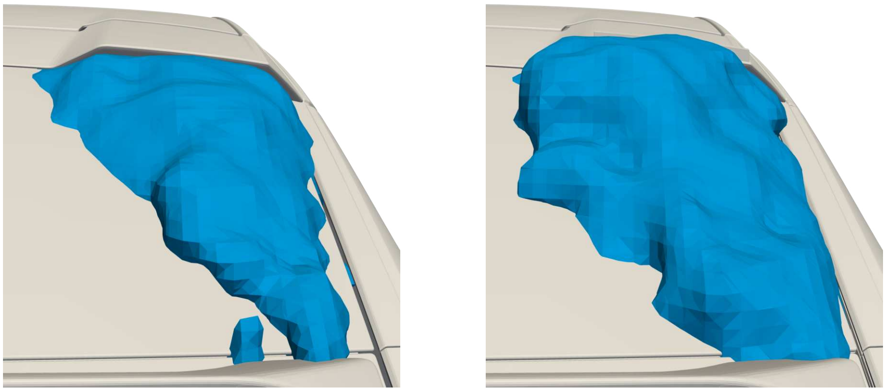

(a) Baseline (b) Roof-kick

Figure 4.20: Isosurfaces $c_{p,tot} = 0$ from the geometrical changes to the roof's separation edge.

Overall, the ProCap measurements clearly capture the differences in flow topology that come from adding the roof-kick.

4.3.2 Removing the rear wing

Removing the rear wing can be seen as a more drastic change than adding the roof-kick, and should therefore result in even larger changes in flow topology. Figure 4.21 shows that this is the case. The most noticeable difference is that the wake is much smaller and more downwashed compared to the baseline. This would lead to the configuration without the rear wing having more rear lift than the baseline.

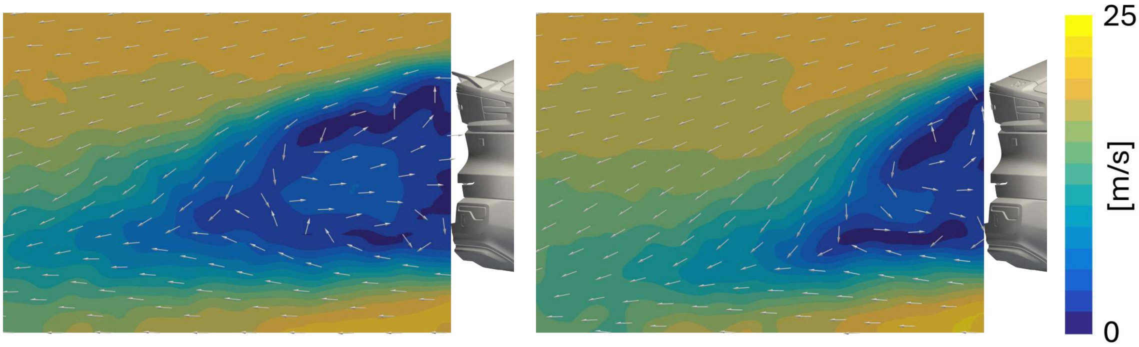

(a) Baseline (b) Removed rear wing

Figure 4.21: The wake's velocity contours for the geometric modification applied.

These two use cases demonstrate the capability of the ProCap system to quickly probe the local flow field to provide real-time insights into the impact of various aerodynamic features. The ProCap system can thereby be used as a complement to simulations to obtain a complete understanding of the local and global flow phenomenon around a test vehicle of interest.

5

Conclusion

The ProCap measurement system was identified as a measurement system bridging the gap between the traditional qualitative and quantitative flow visualization techniques.

From a quantitative perspective, ProCap was found to lack the accuracy and consistency needed for use in CFD method validation. However, qualitatively, the agreements are reasonable. The main difference between ProCap measurements and the traverse-gear-mounted probe or CFD simulations was the ProCap's thickening of the shear layers. This was due to the system relying on a voxel based spatial averaging together with interpolation, which kept the system from being able to resolve steep velocity gradients. Consequently, the delta observed in the ProCap system's repeated measurements, along with its comparison to the TG system, meant it could not serve as a reliable ground truth for CFD validation.

Despite these limitations, ProCap measurements capture the overall flow topology well, particularly in representing the size and approximate shape of flow separations and large-scale flow structures. The topology of rotating structures was also similar between ProCap and CFD simulations. These findings highlight the system's optimal operating domain: visualizing flow separation and reattachment, and providing an approximate representation of the general flow topology. Especially when obtaining unexpected behavior during aerodynamic testing or development, traditionally, smoke or tufts are used because quantitative techniques such as PIV or LDA are considered too time-consuming. In such a scenario, ProCap is a compelling alternative as it can provide significantly more information about the flow than the strictly qualitative methods, but is less time-consuming than the traditional quantitative counterparts.

In conclusion, in terms of accuracy and local flow resolution, the ProCap system surpasses qualitative methods such as smoke and tufts but falls short of traversing-gear-mounted pressure or hot-wire probes, PIV, and LDA. From a complexity and time perspective, the ProCap system can also be considered to be in the middle ground between the purely qualitative and quantitative methods mentioned. ProCap's position within this range can be partially decided by an appropriate choice of voxel size.

Thus, this thesis has demonstrated the typical usability of the ProCap system for use within aerodynamic development.

Bibliography

[1] European Environment Agency, "CO2 emissions performance of new passenger cars in Europe," 2024. [Online]. Available: eea.europa.eu (accessed on: 2025-05-07).

[2] M. Urquhart, "Vehicle Wakes In Side Wind," Lic. thesis, Chalmers University of Technology, Gothenburg, Sweden, 2021. [Online]. Available: research.chalmers.se.

[3] Volvo Car Group, Vehicle Energy Efficiency Department, Internal material.

[4] W.H. Hucho, *Aerodynamik des Automobils.* 1st ed., Würzburg, Germany: Vogel-Druck Würzburg, 1981.

[5] S. Bonitz, "Development of Separation Phenomena on a Passenger Car," Lic. thesis, Chalmers University of Technology, Gothenburg, Sweden, 2018. [Online]. Available: research.chalmers.se

[6] F. Hussain, "On the identification of a vortex," Journal of Fluid Mechanics, vol: 285, Feb 1995, doi: 10.1017/S0022112095000462.

[7] A. Brandt, S. Sebben, and B. Jacobson, "Base wake dynamics and its influence on driving stability of passenger vehicles in crosswind," Journal of Wind Engineering and Industrial Aerodynamics, vol. 230, Nov. 2022, doi: 10.1016/j.jweia.2022.105164.

[8] K. Bajada, "The Aerodynamics of a generic SUV: from optimization to general trends," MSc. Thesis, KTH Royal Institute of Technology, Stockholm, Sweden, 2024. [Online]. Available: kth.diva-portal.org

[9] C. Kounenis et al., "Investigations of the Rear-End Flow Structures on a Sedan Car," SAE Technical Papers, Jan. 2016, doi: 10.4271/2016-01-1606.

[10] A. Buljac, I. Dzijan, I. Korade, s. Krizmanić, and H.Kozmar, "Automobile aerodynamics influenced by airfoil-shaped rear wing," International Journal of Automotive Technology, vol. 17, pp. 377-385, Jun. 2016, doi: s12239-016-0039-4.

[11] R. Rajapaksha, K. Kurukulasooriya, H. Herath, and S. Rangajeeva, "Aerodynamic Analysis of Rear Wings and Rear Spoilers of Passenger Automobiles," in *Annual Sessions of Institution of Engineers*, Sri Lanka, 2018. [Online]. Available: researchgate.net, Accessed on: 2025-05-07.

[12] M. Cakir, "CFD study on aerodynamic effects of a rear wing/ spoiler on a passenger vehicle," MSc. thesis, Santa Clara University, Santa Clara, California, USA, 2012. [Online]. Available: scholarcommons.scu.edu

[13] M. Olsson, "Designing and Optimizing SideView Mirrors," MSc. thesis, Chalmers University of Technology, Gothenburg, Sweden, 2011. [Online]. Available: publications.lib.chalmers.se

[14] S. Prithiviraj and O. Lakshminarayanan, "Aero Acoustic Comparative Study of Conventional and Shark-Fin Antenna," Journal of Applied Science and Computations, vol. 6, pp. 2720-2725, Mar. 2023. Available: reasearchgate.net, Accessed on: 2025-05-07.

[15] P. Ekman, "Important Factors for Accurate Scale-Resolving Simulations of Automotive Aerodynamics," Lic. thesis, Linköping University, Linköping, Sweden, 2020. [Online]. Available: liu.diva-portal.org

[16] M.N. Sudin, M.A. Abdullah, S.A. Shamsudin, and F.R. Ramli, "Review of research on vehicles aerodynamic drag reduction methods," International Journal of Mechanical & Mechatronics Engineering, vol. 14, no. 2, pp 35-47, Apr. 2014. Available: researchgate.net. Accessed on: 2025-05-07.

[17] A.K. Perry, G. Pavia, and M. Passmore, "Influence of short rear end tapers on the wake of a simplified square-back vehicle: wake topology and rear drag," Exp Fluids, vol. 57, no. 169, Oct. 2016, doi: 10.1007/s00348-016-2260-3.

[18] K. He, G. Minelli, J. Wang, and T. Dong, "Numerical investigation of the wake bi-stability behind a notchback Ahmed body," Journal of Fluid Mechanics, vol 926, no. A36, Nov. 2021, doi: 10.1017/jfm.2021.748.

[19] NASA, "Closed Return Wind Tunnel," 2021. [Online]. Available: grc.nasa.gov. Accessed on: 2025-05-07.

[20] NASA, "Open Return Wind Tunnel," 2021. [Online]. Available: grc.nasa.gov. Accessed on: 2025-05-07.

[21] E. Ljungskog, "Evaluation and modeling of the flow in a slotted wall wind tunnel," Lic. thesis, Chalmers University of Technology, Gothenburg, Sweden, 2019. [Online]. Available: research.chalmers.se.

[22] G. S. Manuel and J. K. Molly, "Effect of Collector Configuration on Test Section Turbulence Levels in an Open-Jet Wind Tunnel," NASA, Technical Memorandum 4333, 1992. [Online]. Available: ntrs.nasa.gov. Accessed on: 2025-05-21.

[23] A.A. Rejniak and A. Gatto, "Upstream wind tunnel model mounting: The forgotten method for road vehicle aerodynamics," Proceedings of the Institution of Mechanical Engineers, Part D, vol. 235, no. 7, pp. 1992-2012, 2012, doi: 10.1177/0954407020978017.

[24] E. Mercker and J. Wiedemann, "Comparison of Different Ground Simulation Techniques for Use in Automotive Wind Tunnels," SAE Technical Paper 900321, 1990, doi: 10.4271/900321.

[25] J. Sternéus, T. Walker, and T. Bender, "Upgrade of the Volvo Cars Aerodynamic Wind Tunnel," SAE Technical Paper 2007-01-1043, Jan. 2007, doi: 10.4271/2007-01-1043.

[26] Press release, Volvo Car AB, 2012. [Online]. Available: media.volvocars.com. Accessed on: 2025-05-20.

[27] NASA, "Smoke and Tufts," 2021. [Online]. Available: grc.nasa.gov. Accessed on: 2025-05-07.

[28] Agency for Toxic Substances and Disease Registry, "Public Health Statement for Sulfur Trioxide and Sulfuric Acid," 2014. [Online] Available: cdc.gov. Accessed on: 2025-05-07.

[29] L.H. Tanner and L.G. Blows, "A study of the motion of oil films on surfaces in air flow, with application to the measurement of skin friction," Journal of

Physics E: Scientific Instruments, vol 9, no. 3, Nov 1975, doi: 10.1088/0022-3735/9/3/015.

[30] L.C. Squire, "The motion of a thin oil sheet under the steady boundary layer on a body," Journal of Fluid Mechanics, vol. 11, no. 2, pp. 161-179, Sep. 1961, doi: 10.1017/S0022112061000445.

[31] NASA, "Helicopter Brownout Research". [Online]. Available: rotorcraft.arc.nasa.gov

[32] D. Wieser et al., "Surface Flow Visualization on a Full-Scale Passenger Car with Quantitative Tuft Image Processing," SAE Technical Paper 2016-01-1582, Jan. 2016, doi: 10.4271/2016-01-1582.

[33] N. Omata and S. Shirayama, "Extracting quantitative three-dimensional unsteady flow direction from tuft flow visualizations," Fluid Dynamics Research, vol. 49, no. 5, Aug. 2017, doi: 10.1088/1873-7005/aa8551.

[34] J.O. Bird and P.J. Chivers, *Newnes Engineering and Physical Science Pocket Book*. Oxford, England: Newnes, 1993.

[35] K. Siren, G. Rosén, J. Vad, and P.V. Nielsen, *Industrial Ventilation Design Guidebook*. Cambridge, USA: Academic Press, 2001.

[36] R.T. Adrian, “Twenty years of Particle Image Velocimetry,” Experiments in Fluids, Vol. 39, 2005, pp. 159-169, doi: 10.1007/s00348-005-0991-7.

[37] M. Raffel, C. Willert, S.T. Wereley, and J. Kompenhans, *Particle Image Velocimetry: A Practical Guide*. Springer, 2007.

[38] D.L. Wulff, "PIV Measurements in Pumps. In Design and Analysis of High Speed Pumps" NATO, Educational Notes RTO-EN-AVT-143, Paper 5, Neuilly-sur-Seine, France: RTO, 2006. Available: sto.nato.int. Accessed on: 2025-05-08.

[39] R.W. Johnson et al., "Processes and Procedures for Application of CFD to Nuclear Reactor Safety Analysis," Idaho National Laboratory, Sep. 2006. [Online]. Available: researchgate.net. Accessed on: 2025-05-20.

[40] H. Nobach and E. Bodenschatz, "Limitations of accuracy in PIV due to individual variations of particle image intensities," Exp Fluids, vol. 47, pp. 27–38, 2009, doi: 10.1007/s00348-009-0627-4.

[41] D.R. Neal, A.Sciacchitano, B.L. Smith, and F.Scarano, "Collaborative framework for PIV uncertainty quantification: the experimental database," Measurement Science and Technology, vol 26, no. 7, Jun. 2015, doi: 10.1088/0957-0233/26/7/074003.

[42] S. Adatrao, "Design of experiments A statistical tool for PIV uncertainty quantification," Measurement Science and Technology, vol. 34, no. 1, 2023, doi: 10.1088/1361-6501/ac9541.

[43] F.K.C. Acquah, J.P.K Takyi, and H.R. Beem, "Design and characterization of a low-cost particle image velocimetry system," HardwareX, vol. 19, Sep. 2024, 10.1016/j.ohx.2024.e00563.

[44] Vrije Universiteit Amsterdam, "Experimental design and measurement". [Online]. Available: nat.vu.nl. Accessed on: 2025-05-20.

[45] W. Jian, "Development of the primary velocity standard for the calibration of LDA system," Measurement in Research and Industry, XXI IM EKO World Congress, Prague, Czech Republic, Sep. 2015. [Online]. Available: imeko.info. Accessed on: 2025-05-13.

[46] C.J. Crowley et al., "Calibrating laser Doppler anemometers utilizing an optical chopper," Metrologia, vol. 62, no. 2, 2025, doi: 10.1088/1681-7575/adac64.

[47] D.A. Johnson, "Laser Doppler Anemometry," NASA, Technical Memorandum 100072, Jun. 1988. [Online]. Available: ntrs.nasa.gov. Accessed on: 2025-05-13.

[48] C.O. Brown, "Henry Darcy and the Pitot Tube," Third National Congress on Civil Engineering History and Heritage, Oct 2001, doi: 10.1061/40594(265)43.

[49] Y. Huang et al., *Industrial Ventilation Design Guidebook*, 2nd ed., Cambridge, USA: Academic Press, 2021.

[50] I. Jonsson and B. Legrady, "Multi-hole probe: A Review and a New Take to Improve Accuracy," unpublished. doi: 10.21203/rs.3.rs-4801492/v1.

[51] D. Telionis, Y Yang, and O. Rediniotis, "Recent Developments in Multi-Hole Probe (MHP) Technology," 20th International Congress of Mechanical Engineering, Brazil, Nov. 2009. [Online]. Available: abcm.org. Accessed on: 2025-06-02.

[52] Vectoflow, "Conventional multi-hole probes." [Online]. Available: vectoflow.de. Accessed on: 2025-06-02.

[53] S.B. Pope, *Turbulent Flows*, 1st ed., Cambridge, USA: Cambridge University Press, 2000.

[54] E.M.V. Siggeirsson, "Aerodynamics of an Aeroengine Intermediate Compressor Duct: Effects from an Integrated Bleed System," Lic. thesis, Chalmers University of Technology, Gothenburg, Sweden, 2020. [Online]. Available: research.chalmers.se.

[55] W.K. George, "Lectures in Turbulence for the 21st Century," Department of Aeronautics, Imperial College of London, London, UK, Jan 2013. [Online]. Available: turbulence-online.com. Accessed on: 2025-05-13.

[56] P. Moin and K. Mahesh, "Direct Numerical Simulation: A Tool in Turbulence Research," Annual Review of Fluid Mechanics, vol. 30, no. 1, pp. 539-578, Jan. 1998, doi: 10.1146/annurev.fluid.30.1.539.

[57] C. Mockett, "A comprehensive study of detached-eddy simulation," Lic. thesis, Technical University of Berlin, Berlin, Germany, 2009. [Online]. Available: researchgate.net.

[58] N.J. Georgiadis, D.P. Rizzetta, and C. Fureby, "Large-Eddy Simulation: Current Capabilities, Recommended Practices, and Future Research," AIAA Journal, vol. 48, no. 8, pp. 1772-1784, doi: 10.2514/1.J050232.

[59] E. Ljungskog, "Investigations of Flow Conditions in an Automotive Wind Tunnel," Lic. thesis, Chalmers University of Technology, Gothenburg, Sweden, 2017. [Online]. Available: publications.lib.chalmers.se

[60] A. Müller, "Real-Time 3D Flow Visualization Technique with Large Scale Capability," Lic. thesis, ETH Zürich, Zürich, Switzerland, 2017. [Online]. Available: research-collection.ethz.ch.

[61] J. Bartl et al.,"Validation of the real-time-response ProCap measurement system for full field wake scans behind a yawed model-scale wind turbine," Journal of Physics: Conference Series, vol. 1104, 2018, doi: 10.1088/1742-6596/1104/1/012018.

[62] B. Rembold, "Accelerating Aerodynamic Design: Fast Analysis Tools," Airshaper, 2022. [Online]. Available: procap.tech. Accessed on: 2025-05-14.

[63] B. Rembold, "3D Flow Measurement in the Wind Tunnel - A Formula Student Case Study," AirShaper. [Online]. Available: airshaper.com. Accessed on: 2025-05-14.

[64] E. Josefsson, F.F. Semeraro, M. Urquhart, and S. Sebben, "Investigation of tyre rim protectors on the aerodynamics of a passenger vehicle," Experiments in Fluids, vol. 65, no. 5, Apr. 2024, doi: 10.1007/s00348-024-03805-0.

[65] E. Josefsson, " Tyre aerodynamics of passenger vehicles," Lic. thesis, Chalmers University of Technology, Gothenburg, Sweden, 2022. [Online]. Available: research.chalmers.se.

[66] D. De Jourday, "An Experimental Investigation of the Boundary Layer Control System of Volvo's Slotted Wall Automotive Wind Tunnel," MSc thesis, KTH, Stockholm, Sweden, 2025. [Online]. Available: kth.diva-portal.org

DEPARTMENT OF MECHANICS AND MARITIME SCIENCES
CHALMERS UNIVERSITY OF TECHNOLOGY
Gothenburg, Sweden 2025
www.chalmers.se

CHALMERS
UNIVERSITY OF TECHNOLOGY